Published in final edited form as:
Nature. 2022 July 01; 607(7920): 790–798. doi:10.1038/s41586-022-04924-6.

YAP/TAZ activity in stromal cells prevents ageing by controlling cGAS-STING

Hanna Lucie Sladitschek-Martens[#1], **Alberto Guarnieri**[#1], **Giulia Brumana**[1], **Francesca Zanconato**[1], **Giusy Battilana**[1], **Romy Lucon Xiccato**[1], **Tito Panciera**[1], **Mattia Forcato**[2], **Silvio Bicciato**[2], **Vincenza Guzzardo**[3], **Matteo Fassan**[3], **Lorenzo Ulliana**[4], **Alessandro Gandin**[4], **Claudio Tripodo**[5,6], **Marco Foiani**[6,7], **Giovanna Brusatin**[4], **Michelangelo Cordenonsi**[1], **Stefano Piccolo**[1,6,*]

[1]Department of Molecular Medicine, University of Padua, Padua, Italy

[2]Department of Life Sciences, University of Modena and Reggio Emilia, Modena, Italy

[3]Department of Medicine, University of Padua, Padua, Italy

[4]Department of Industrial Engineering, University of Padua, Padua, Italy

[5]Department of Health Sciences Unit, Human Pathology Section, University of Palermo, Italy

[6]IFOM ETS, the AIRC Institute of Molecular Oncology

[7]University of Milan, Milan, Italy

[#] These authors contributed equally to this work.

Abstract

Ageing has been causally linked to the induction of cell senescence[1,2], but why this is so remains poorly understood. A key challenge is the identification of pathways that normally suppress senescence, are lost during ageing and are functionally relevant to oppose ageing[3]. Here we connected the structural and functional decline of ageing tissues to attenuated function of the master effectors of cellular mechanosignalling YAP and TAZ. YAP/TAZ activity declines during physiological ageing in stromal cells, and mimicking such decline through genetic inactivation of YAP/TAZ leads to accelerated ageing. Conversely, sustaining YAP function rejuvenates old cells and opposes the emergence of ageing-related traits associated with either physiological

---

[*] Correspondence should be addressed to: Stefano Piccolo, Department of Molecular Medicine, University of Padua, viale Colombo 3, 35100 Padua, Italy, IFOM ETS, the AIRC Institute of Molecular Oncology, via Adamello 16, 20139 Milano, Italy, TEL 0039049 8276098, FAX 0039049 8276079, piccolo@bio.unipd.it.

Authors' contributions

H.L.S.-M., G.Brumana, A.Guarnieri performed most of the experiments *in vitro* and *in vivo*, and contributed to the writing. F.Z. and G.Battilana carried out single-cell analyses and ChIP-PCR. M.Forcato, S.B. and M.C. provided the bioinformatic data. V.G. carried out histology. M.Fassan performed histopathological evaluations. T.P helped with the mouse colonies. A.Gandin, L.U. and G. Brusatin supported the mechanical bioassays. RLX helped with Remodelin. M. Foiani provided advice and reagents for cGAS. C. Tripodo performed PLA. All authors contributed to the MS. S.P. conceived the initial hypothesis and experimental design, organized the work and wrote the MS.

Competing interests

The authors declare no competing interests.

Rights and permissions

Correspondence and requests for materials, and informations regarding reprints and permissions should be addressed to S.P.

ageing or accelerated ageing triggered by a mechano-defective extracellular matrix. Ageing traits induced by inactivation of YAP/TAZ are preceded by induction of tissue senescence. This occurs because YAP/TAZ mechanotransduction suppresses cGAS-STING signalling, to the extent that inhibition of STING prevents tissue senescence and premature ageing-related tissue degeneration after YAP/TAZ inactivation. Mechanistically, YAP/TAZ-mediated control of cGAS-STING signalling relies on the unexpected role of YAP/TAZ in preserving nuclear envelope integrity, at least in part through direct transcriptional regulation of LaminB1 and ACTR2, the latter of which is involved in building the peri-nuclear actin cap. The findings demonstrate that declining YAP/TAZ mechanotransduction drives ageing by unleashing cGAS-STING signalling, a pillar of innate immunity. Thus, sustaining YAP/TAZ mechanosignalling or inhibiting STING may represent promising approaches for limiting senescence-associated inflammation and improve healthy ageing.

Introduction

A large body of contributions has revealed several hallmarks of ageing[3], and a major challenge in ageing research is to distinguish which age-related alterations play a driving role in this process, whether these alterations occur in a sequential order, and how they are connected. A key challenge is the identification of genes and pathways that are lost during physiological ageing and that functionally serve as suppressors of ageing. It is widely believed that ageing ultimately implies dysregulated transcriptional control[3]. However, the identity of endogenous transcription factors and related signalling pathways that are required to control the balance of youthfulness and ageing in an adult body remains unclear.

Ageing has been associated with cellular senescence, a process that results in growth arrest and expression of a distinctive proinflammatory, secretory phenotype[1]. Elegant “senolytic” approaches have showed that the accumulation of senescent cells is a central driver of ageing-related tissue degeneration[2]. It is unclear, however, whether senescence begins in specific cell types, and what induces this cell state in the first place. The link between ageing, senescence and inflammation indicates that ageing is also intertwined with non-cell autonomous, maladaptive changes in how cells communicate with each other and their surrounding extracellular matrix (ECM)[3]. Of note, young stromal cells have been shown to rejuvenate old stem cells[4], while an old microenvironment readily “ages” young stem cells[5], reinforcing the view that ageing is rooted to dysfunctions in the cellular context. Pondering on the nature of these dysfunctions, here we considered that the “wear- and-tear” of living tissues during ageing, so intimately associated with their structural and functional decline, could be molecularly redefined as declining cellular mechanotransduction. Mechanotransduction is the process by which cells sense the physical, mechanical and architectural properties of their microenvironment[6,7]. A wealth of studies has shown that mechanical signals are transduced by the YAP/TAZ transcriptional coactivators, by Hippo-dependent and -independent mechanisms, into gene-expression programs[7,8], thereby linking mechanical signals to cell behavior. Thinking along these lines, here we investigated the in vivo role of YAP/TAZ in the control of ageing.

We first monitored the status of YAP/TAZ activity during physiological ageing by carrying out single-cell RNA-seq of the dermis of young vs. old mice. Intriguingly, querying these fibroblast populations with a broadly used signature of YAP/TAZ activity (Cordenonsi_YAP_conserved gene set)[9], we found that YAP/TAZ function remarkably declines during ageing (Fig. 1a). To extend this conclusion, we used *Tabula Muris Senis*[10], a compendium of single-cell transcriptomic data of multiple organs, which allowed us to monitor the dynamics of YAP/TAZ activity across the mouse lifetime. These data also showed that endogenous YAP/TAZ activity becomes attenuated during ageing. Notably, however, this decline is not a generalized feature shared by all cell types, but occurs primarily in stromal cells, such as in fibroblasts (the cells that provide a structural framework to mammalian organs[11]) or in professional contractile cells such as vascular smooth muscle cells (vSMCs) and cardiomyocytes, whose biology is embedded in mechanics[12] (Fig. 1b and Extended Data Fig. 1a). By contrast, ageing does not appear to erode YAP/TAZ activity levels in other cell types, such as epithelial cells, neurons or lymphocytes (Extended Data Fig. 1b).

To investigate more directly the dynamic of YAP/TAZ activity during ageing, we first focused our attention on the stromal cells of the skin, the largest organ of a mammalian body and a model for ageing research. We carried out YAP/TAZ immunofluorescence (IF) analyses in the dermis of 3-, 12-, 15-, 18- and 22-month-old mice. As established by proxy of YAP/TAZ activity, we assessed in individual cells the nuclear versus cytoplasmic YAP/TAZ localization (reflecting their ON versus OFF state, respectively)[6]. We found that nuclear YAP/TAZ localization peaks in the young dermis, but has declined by middle age to become essentially undetectable in the old dermis (Fig. 1c, d). As a second model, we focused on the thoracic aorta, which is physiologically exposed to the mechanical strains of the pulsating blood flow and whose medial degeneration is a hallmark of age-related vascular pathology[12]. Monitoring YAP/TAZ localization over time in aortic vSMCs, we found that, again, YAP/TAZ nuclear localization is highest in young mice and progressively declines as ageing proceeds (Fig. 1e, f). Of note, using western blot of lysates from both dermis and aortic media, we found that these changes are independent of the Hippo pathway, as the amount of phospho-YAP is constitutive and unaffected by ageing (Extended Data Fig. 1c).

To directly probe age-related changes in the mechanical state of stromal cells, we used immunofluorescence to monitor at different ages the phosphorylation status of MLC2, a marker reflecting the tensional state of the actomyosin cytoskeleton[7] (Fig. 1g-j). We also used p-FAK to monitor the activation state of integrins, also known to require inner pulling forces mediated by actomyosin tension[12] (Extended Data Fig. 1d-g). The number of cells actively engaged by mechanical forces decreases with ageing, mirroring the decline in YAP/TAZ. Collectively, the data suggest that ageing associates to a progressive decrease in YAP/TAZ mechanosignalling.

The above results prompted us to investigate the causal connections between YAP/TAZ function and the ageing process. To experimentally mimic the decline of YAP/TAZ activity during physiological ageing, we carried out YAP/TAZ inactivation in stromal cells of young adult mice. For this, we first combined YAP/TAZ conditional alleles ($YAP^{fl/fl};TAZ^{fl/fl}$) with

Collagen1a2 (Col1a2)-CreER[13], an established driver that is active in adult fibroblasts of the dermis (Extended Data Fig. 2a) (hereafter Col-YAP/TAZ cKO mice). YAP/TAZ were genetically deleted by Tamoxifen administration at 2.5 months of age, and mice were analyzed after 5-8 weeks (see Methods). Histopathological assessment of the skin of young Col-YAP/TAZ cKO mice showed a decreased number of fibroblasts (Fig. 2a, b and Extended Data Fig. 2b), upregulation of *Cdkn1a* mRNA (Fig. 2c and Extended Data Fig. 2c), and aberrant collagen deposition (Extended Data Fig. 2d, e), all established phenotypes of the ageing dermis[11,14]. YAP/TAZ ablation in dermal fibroblasts also led to non-cell-autonomous effects, such as reduction of subcutaneous fat and reduced density of hair follicles (Fig. 2d), well-known traits of the ageing skin[15]. In addition, the phenotype of Col-YAP/TAZ cKO mice overlaps with that of old mice (>21 months) (Fig. 2a-d and Extended Data Fig. 2b-e). Together with the decline of YAP/TAZ mechanosignalling during physiological ageing, these genetic findings suggest that YAP/TAZ activity in stromal cells is a key factor to prevent premature emergence of ageing-related tissue degeneration.

Next, we investigated at single-cell resolution the extent of the overlap between the transcriptomes of YAP/TAZ cKO and naturally aged dermal fibroblasts. We compared scRNA-seq data for the dermis of young control mice (3 months) with that of young YAP/TAZ cKO (4 weeks after Tamoxifen treatment) or old control mice (24 months). Remarkably, about 75% of genes downregulated in old dermal fibroblasts were also downregulated after YAP/TAZ cKO; consistently, 50% of genes upregulated during ageing were also upregulated after YAP/TAZ cKO (Fig. 2e). Thus, single-cell transcriptomics of dermal fibroblasts indicates that natural ageing and YAP/TAZ-deficiency converge toward largely overlapping transcriptional landscapes (Fig. 2e and Extended Data Fig. 2f).

In light of the above results on YAP/TAZ cKO mice, and given that declining YAP/TAZ activity accompanies physiological ageing, we next asked whether the converse experiment - experimentally sustaining YAP/TAZ activity - could delay or suppress features of ageing. For this, we used mice carrying a doxycycline-inducible transgene encoding active YAP (*TetO-YAPS127A;R26-rtTAM2*)[16]; starting from 3 months of age, mice were kept under a pulsating regimen of YAP expression (as measured by western blot on tail tip fibroblasts, Extended Data Fig. 2g) by administering low doses of doxycycline twice a week until they reached more than 21 months of age. We found that sustaining YAP function prevented several features of ageing, rescuing fibroblast density (as visualized by histology in Fig. 2a, b, and quantified from Vimentin staining in Extended Data Fig. 2b), collagen organization (as visualized by birefringence of Picrosirius Red staining Extended Data Fig. 2d, e), *Cdkn1a* mRNA expression (Fig. 2c and Extended Data Fig. 2c) and hair follicle density (Fig. 2d), all to levels comparable to those of younger mice.

We next extended these conclusions to a second example of declining YAP/TAZ mechanosignalling during ageing, that is the aortic wall (as per Fig.1). We tested whether experimentally phenocopying of such a decline would cause accelerated ageing in this context. To this end, we carried out conditional YAP/TAZ genetic ablation, by generating a mouse strain combining $YAP^{fl/fl};TAZ^{fl/fl}$ with $Smmhc\text{-}CreER^{T2}$, a well-established driver expressing Tamoxifen-regulated Cre specifically in SMCs[17] (hereafter SMC-YAP/TAZ cKO mice) (Extended Data Fig. 3a). Specific YAP/TAZ deletion could be observed in

SMC-YAP/TAZ cKO adult mice after 5 days of Tamoxifen administration (Extended Data Fig. 3b). From 6 weeks, SMC-YAP/TAZ cKO mice started to suddenly die; necropsies (n=8) revealed massive thoracic hemorrhages with histological evidence of aortic dissection and rupture. At earlier time points, histological analyses of all mice (n=23) showed clear changes in the aortic architecture, such as increased medial thickening, alterations in SMC morphology and elastic fiber fragmentation that were essentially indistinguishable from those detected in aged mice (Fig. 3a, quantified in Extended Data Fig. 3c). Thus, YAP/TAZ mechanotransduction in aortic SMCs is an essential signal integral to the youthful homeostasis of the aortic wall, and its attenuation drives pathological features typically associated with natural ageing.

If YAP/TAZ mechanotransduction is relevant for controlling the ageing process, then attenuating mechanotransduction through direct manipulation of the ECM should also favor the emerge of ageing phenotypes, and in a manner driven by YAP/TAZ inhibition. An ideal playground to test this hypothesis is represented by mutations in *Fbn1*, which encodes Fibrillin-1 - an adhesive protein associated with the elastic fibers. *Fbn1* mutations are linked to aortic aneurysm formation and Marfan syndrome[18]. It has been recently proposed that these defects represent a tissue-specific form of accelerated ageing of the aortic wall[19]. Indeed, the aortic histopathologies of aged mice (>21 months) and Fibrillin1 mutant (Fbn1$^{C1039G/wt}$) mice (at 7 months of age) largely overlap, displaying increased medial thickening, adventitial enlargement, elastic fiber fragmentation and disarray invariably leading to aneurysm (Fig. 3b, quantified in Extended Fig. 3c). Dysfunctional mechanosensing has been suggested as primary driver of aortic aneurysms[12] and associated to Fbn1 mutation[18]; indeed, young Fbn1 mutants are ostensibly normal, yet, over adult life, vSMC-ECM adhesion rapidly falls below threshold required for vascular wall homeostasis[20]. We investigated whether the accelerated aortic ageing of Fbn1 mutants is accompanied by accelerated loss of nuclear YAP/TAZ and cytoskeletal tension. As visualized by immunofluorescence for YAP/TAZ, p-MLC2 and by western blot for p-FAK, we found that *Fbn1* mutation recapitulates, in a few months, the mechanosensing decline that normally occurs over a lifetime (Fig. 3c, d and Extended Data Fig. 3d-f). To test whether this accelerated decline of YAP/TAZ activity is causal of the aortic ageing phenotype of *Fbn1* mutants, we crossed *Fbn1*$^{C1039G/WT}$ mice with transgenic mice expressing a doxycycline-inducible, active form of YAP specifically in vSMCs (that is, *Smmhc-CreER*^{T2}*;LSL-rtTA;TetO-YAPS127A* mice) and induced YAP expression at 5 months of age for 2 months. While in untreated Fbn1 mutant mice aortic pathology progressed strongly in this time window, adding back YAP had a remarkable effect, preventing medial and adventitial thickening and elastic lamellae degradation and thereby completely stopping progression toward ageing-like tissue degeneration (Fig. 3e, f and Extended Data Fig. 3g).

The data presented so far start to paint a picture in which YAP/TAZ mechanotransduction in stromal cells is critical to prevent ageing, but the nature of the YAP/TAZ youth-preserving functions is unclear. To start answering this question, we carried out whole-transcriptome analyses to capture gene-expression changes induced early on after genetic ablation of YAP/TAZ. For this, we cultured freshly explanted dermal fibroblasts from young control and *R26-CAG-CreER; Yap*$^{fl/fl}$*; Taz*$^{fl/fl}$ mice, and compared the two populations by RNA-seq after 48 h of 4-hydroxytamoxifen treatment *in vitro*. Gene-set enrichment analyses (GSEA) revealed that the genes induced after YAP/TAZ knockout are enriched in a number of redundant signatures defining a proinflammatory cell state, known as Senescence-Associated Secretory Phenotype[1] (SASP) (Supplementary Table 1 and Extended Data Fig. 4a); we validated this at the secretome level by cytokine arrays (Extended Data Fig. 4b). Supporting the generality of these findings, SASP was also induced in human fibroblasts and mouse aortic vSMCs after YAP/TAZ inactivation (Extended Data Fig. 4c, d). Of note, SASP induction upon YAP/TAZ inactivation occurs also after treatment with CDK4/6 inhibitor, that is, irrespectively of cell proliferation (Extended Data Fig. 4e). Loss of YAP/TAZ in cultured fibroblasts also activates senescence-associated β-Galactosidase (SA-β-Gal), a classic marker of senescence (Extended Data Fig. 4f), consistent with prior in vitro findings[21].

A role of YAP/TAZ in controlling cell senescence was intriguing in light of the connection between YAP/TAZ and ageing, since emergence of senescent cells has been proposed to be causal to age-related tissue dysfunctions[1,2]. Senescence is also a feature of old fibroblasts in vitro[11]. We found that old fibroblasts, analyzed shortly after explantation, retain the same cytoplasmic YAP/TAZ bias they display in vivo (Fig. 4a); notably, experimentally sustaining YAP/TAZ activity rejuvenated these cells, suppressing SASP and SA-β-Gal expression (Fig. 4b, Extended Data Fig. 4g,h). SASP suppression was also attained by sustaining endogenous mechanotransduction and YAP/TAZ nuclear levels, through treatment with the integrin agonist pyrintegrin[22] (Extended Data Fig. 4i, j). Conversely, senescence was readily induced in young fibroblasts by experimental attenuation of YAP/TAZ mechanotransduction through inhibition of Rho-GTPases (Extended Data Fig 4k, l), one of the key upstream inputs that, by modulating the actin cytoskeleton, positively controls YAP/TAZ activity[6]. Thus, induction of senescence in old fibroblasts functionally associates to declining YAP/TAZ function.

The upregulation of a SASP-related program after YAP/TAZ inactivation hinted at the possibility that YAP/TAZ normally inhibit unscheduled activation of a signalling cascade that orchestrates SASP. We asked what this pathway could be, and whether we may use it to interfere with the accelerated ageing of YAP/TAZ cKO mice. Several studies identified the cGAS-STING cascade as a leading inducer of SASP *in vitro* and of an inflammatory milieu *in vivo* in the context of autoimmune disease models[23–26]. cGAS is part of the innate immune response, serving as major receptor of cytoplasmic DNA in mammalian cells, including endogenous nuclear DNA made accessible to the cytoplasm after loss of nuclear envelope (NE) integrity[25]. Once activated, cGAS produces cGAMP as a second messenger, in turn stimulating STING and downstream transcriptional effects[25,26]. cGAS activation has been so far mainly considered in cells challenged with DNA damaging agents, or in the context of oncogene-induced senescence[25,26]. However, much less is known on the endogenous factors that regulate cGAS-STING signalling under physiological conditions *in vivo*, including cues emanating from the cell's microenvironment.

We thus investigated whether YAP/TAZ mechanotransduction could serve as barrier against unscheduled cGAS-STING activation. We directly addressed this first by quantifying cGAMP in freshly explanted young dermal fibroblasts and vSMCs after *ex vivo* YAP/TAZ genetic ablation. YAP/TAZ knockout cells showed massive upregulation of cGAMP, in a manner that could be rescued by concomitant cGAS downregulation (Fig. 4c and Extended Data Fig. 5a). At the cell biology level, an established and immediate read-out of cGAS activation is its accrual at discrete, subcellular spots. We detected endogenous cGAS accrual at the nuclear-cytoplasmic border, and in nuclear "herniations" in the cytoplasm of YAP/TAZ-depleted primary fibroblasts (Fig. 4d and Extended Data Fig. 5b). To support this finding, we also used WI-38 fibroblasts stably expressing enhanced fluorescent protein (EGFP)-cGAS, an established sensor of cGAS activity. In control cells, the EGFP-cGAS signal was evenly distributed in the cell cytoplasm; siRNA-mediated depletion of YAP/TAZ caused massive accrual of EGFP-cGAS inside the nucleus, at the nuclear-cytoplasmic border, and in nuclear "herniations" (Extended Data Fig. 5c). We also carried out 3D reconstruction from super-resolution microscopy to finely appreciate the localization of EGFP-cGAS in YAP/TAZ depleted cells, and found it recruited onto exposed genomic DNA (DAPI staining) at sites of nuclear envelope rupture (Fig. 4e and Extended Data Fig. 5d).

Consistent with these *in vitro* experiments, we also found *in vivo* nuclear and perinuclear accrual of endogenous cGAS after YAP/TAZ KO in dermis and aortic wall (Fig. 4f, g and Extended Data Fig. 5e, f). We further extended these analyses to the kidney, in which the *Col1a2-CreER* driver is also active in glomerular mesangial cells[13], where we found activation of endogenous cGAS after YAP/TAZ cKO (Extended Data Fig. 5g). Next, we validated that the bright spots of cGAS accrual in YAP/TAZ cKO tissues colocalize with DNA. For this, we combined antibodies against cGAS and DNA in Proximity Ligation Assays (PLA), a method that allows *in situ* detection of closely associated molecules. PLA-positive signals of endogenous cGAS-DNA interactions were invariably found at the nuclear border of cells from YAP/TAZ cKO tissues, but not from control mice (Extended Data Fig. 5h).

Next, we investigated the role of mechanical cues in the regulation of the YAP/TAZ-cGAS axis. For this, we inhibited YAP/TAZ activity by plating fibroblasts on compliant ECM-hydrogels, as such reducing the pulling forces from the ECM[6]. Mechanical inhibition of YAP/TAZ led to activation of cGAS, which was indeed rescued by adding back YAP (Extended Data Fig. 6a,b). Similarly, in another model of low tensional state (cellular confinement onto small adhesive areas[6]), mechanical inhibition of endogenous YAP/TAZ also triggered activation of cGAS (Extended Data Fig. 6c); under these conditions, cells are forced to adopt a more rounded morphology, a phenomenon that has also been observed in human dermal fibroblast during ageing[11,14]. Thus, cGAS regulation is under the controlled by cellular mechanotransduction through YAP/TAZ. We also showed that cGAS is under the control of YAP/TAZ mechanotransduction in vivo: mechano-defective, *Fbn1*-mutant aortic wall cells show cGAS accrual and induction of cell senescence (Extended Data Fig. 6d,e). This follows YAP/TAZ mechanical inhibition in these experimental conditions (Fig. 3c,d), to the extent that these responses are abolished by adding back YAP (Extended Data Fig. 6d,e).

Next, we aimed to causally connect cGAS-STING signalling to the control of senescent phenotypes by YAP/TAZ. We first addressed this issue in vitro, comparing the transcriptome of YAP/TAZ-depleted WI-38 fibroblasts in absence or presence of concomitant depletion of cGAS or STING. Strikingly, about a quarter (23%) of genes upregulated by YAP/TAZ inactivation is cGAS- and STING-dependent, indicating that suppression of unscheduled cGAS-STING activation accounts for a relevant fraction of YAP/TAZ biology in these cells. Importantly, SASP genes and typical type I Interferon-stimulated genes (also well known to be induced by cGAS-STING) belong to this fraction (Fig. 4h and Extended Data Fig. 7b). We extensively validated that YAP/TAZ inactivation causes activation of this gene-responses through cGAS by RT-qPCR in human fibroblasts, using YAP/TAZ siRNA in combination with independent siRNAs for cGAS or STING (Supplementary Table 2). Reinforcing the above conclusion, we could ascertain a remarkable epistatic relationship between YAP/TAZ and cGAS-STING for a large fraction of genes previously classified as inflammatory response genes, such as NF-kB targets and interferon-activated genes (Extended Data Fig. 7a-c). In contrast, STING depletion was inconsequential for the regulation of genes related to YAP/TAZ-mediated proliferation (Extended Data Fig. 7d), in line with the notion that a plethora of proliferative control genes are directly transcriptionally regulated by YAP/TAZ[27]. Similar conclusions were also obtained in primary dermal fibroblasts or vSMCs, whereby STING inactivation prevented SASP induced by YAP/TAZ downregulation (Extended Data Fig. 7e-h). By *in situ* hybridization (ISH) in individual YAP/TAZ-depleted cells, expression of the SASP marker *CXCL10* was specifically upregulated in cells displaying nuclear accrual of cGAS (Extended Data Fig. 7i). We conclude that cGAS-STING signalling is causal for the regulation of SASP by YAP/TAZ.

A key question in ageing research relates to the identity of the mechanisms that induce senescence in living tissues. In this context, the role of cGAS-STING signalling as conduit to ageing through promotion of in vivo senescence remains largely underinvestigated[26]. The present discovery of the YAP/TAZ-cGAS-STING axis may contribute to these outstanding issues, prospecting a scenario in which declining YAP/TAZ levels may trigger aberrant cGAS and STING activation in vivo to induce first senescence and then ageing. To genetically address this notion, we compared YAP/TAZ cKOs with triple mutants in which conditional inactivation of YAP/TAZ was coupled to a homozygous inactivating mutation in *Sting* (T596A[28]; hereafter *STING*$^{Gt/Gt}$). We found that YAP/TAZ inactivation caused notable accumulation of senescent cells, as assessed by ISH in dermal fibroblasts, or by RT-qPCR in aortic wall explants. Strikingly, these senescent phenotypes were completely prevented by concomitant STING inactivation (Fig. 4i, j and Extended Data Fig. 8a-d). STING-dependent accrual of senescent cells was also validated in stromal cells of the kidney after YAP/TAZ cKO (Fig. 4k and Extended Fig. 8e, f). It is worth noting that induction of STING-dependent senescence traits occurs in vivo just over 2 weeks after YAP/TAZ conditional inactivation, that is, well before the onset of any age-related histopathological manifestations in the same tissues. Loss of STING recovered also all the premature ageing traits induced by YAP/TAZ loss in young tissues (Fig. 4l, m). Indeed, in the skin of YAP/TAZ cKO; *STING*$^{Gt/Gt}$ mice, STING inactivation prevented loss of fibroblasts and preserved youthful ECM organization, subcutaneous fat layer and hair follicle density (Extended Data Fig. 8g). In the aorta, STING inactivation prevented medial thickening and elastic fiber fragmentation, as assessed genetically (SMC-YAP/TAZ cKO; *Sting*$^{Gt/Gt}$ mice), or after administration of the STING inhibitor C-176[29] to SMC-YAP/TAZ cKO mice (Extended Data Fig 8h-j). In the kidney, conditional YAP/TAZ inactivation leads to glomerulosclerosis and tubular atrophy (Fig. 4n and Extended Data Fig. 8k, l), and these histopathological traits typical of the ageing kidney were also completely rescued by loss of STING. Taken together, these data indicate that YAP/TAZ restrain cGAS-STING signalling during adult tissue homeostasis *in vivo*, preventing emergence of senescent cells, of a proinflammatory microenvironment and age-related tissue dysfunction.

As the final element of this work, we focused on the mechanism by which YAP/TAZ restrain cGAS-STING signalling. The findings shown above in Fig. 4, on the loss of YAP/TAZ causing cGAS accrual at sites of NE discontinuities, raised the tempting possibility that YAP/TAZ may serve as safeguards of NE architecture. Alterations in nuclear envelope shape and composition have been reported to occur during ageing in human fibroblasts in vitro[11]. Consistently, we found that freshly explanted old mouse fibroblasts also display severely distorted nuclear shape, and that these defects could be rescued by YAP add-back (Fig. 5a and Extended Data Fig. 9a), paralleling the ability of exogenous YAP to inhibit SASP in these cells (for example, Fig. 4b). In line with this, more than 50% of YAP/TAZ-depleted fibroblasts displayed a host of nuclear defects, such as wrinkles, indentations, lobulations of the NE, and increased nuclear height (Fig. 5a, left panels and Extended Data Fig. 9a-d). YAP/TAZ inhibition by low mechanics, by either soft ECM or cell confinement, also dramatically altered nuclear morphology (Extended Data Fig. 9e,f).

These observations prompted us to investigate whether, in YAP/TAZ-depleted cells, fragility of the NE, reflecting in NE ruptures and dysmorphia, is causal for the cGAS-mediated SASP activation. To address this, we treated YAP/TAZ-depleted cells with Remodelin, a small molecule that has been shown to rescue nuclear shape, and to ameliorate premature ageing pathologies of progeroid mice through normalization of NE-cytoskeletal iinteractions[30]. We found that Remodelin indeed rescues normal nuclear shape in YAP/TAZ-depleted cells, also blunting cGAS accrual and SASP induction (Fig. 5b and Extended Data Fig. 9g-j).

Recent work has indicated that, particularly in fibroblasts, the shape of the nucleus is tightly regulated by a dome-like structuring of F-actin filaments, called the perinuclear actin cap, that wraps around the apical surface of the nucleus, keeping the NE smoothly distended and preventing its deformation[31,32]. Actin cap filaments directly connect to the NE, in part through the LINC complexes[33], forming a structural continuum between the cytoskeleton and the NE. We therefore investigated whether YAP/TAZ are required for the assembly of the actin cap. In vivo, confocal imaging of tissue sections stained with phalloidin revealed that YAP/TAZ cKO fibroblasts display remarkable loss of the perinuclear F-actin wrap compared to cells in young control tissues (Extended Data Fig. 9k). Similarly, in vitro, the actin cap was lost upon YAP/TAZ-depletion in young fibroblasts, and in explanted old fibroblasts; notably, the impaired YAP/TAZ status of these cells is causal for this event since the actin cap structure was restored in old cells by sustaining YAP activity (Fig. 5c and Extended Data Fig. 10a). Moreover, restoration of NE integrity by Remodelin treatment also rescued the actin cap in YAP/TAZ-depleted cells (Extended Data Fig. 10b), paralleling the suppression of cGAS accrual and SASP induction by this treatment.

If YAP regulates nuclear shape through the actin cap then interfering directly with the actin cap should mimic the effects of YAP/TAZ depletion on NE integrity, cGAS activation and induction of senescence. We found that interfering with the F-actin-nuclear connections by specifically targeting the LINC complex[34] through the expression of dominant-negative KASH domain or depletion of nesprin1/2 or SUN1/2 was sufficient to induce nuclear wrinkling and bulging, cGAS activation and transcription of SASP markers in a STING-dependent manner (Fig. 5d, Extended Data Fig. 10c-f). Also mimicking the effects of YAP/TAZ depletion, disruption of the actin cap correlated with a high degree of nuclear dysmorphia in cells transfected with anti nesprin1/2 siRNAs (Extended Data Fig. 10g). This indicates that, downstream to YAP/TAZ, the structural continuum between the NE and the cytoskeleton is causal to prevent cGAS-STING signalling.

The results so far indicate that at the core of YAP/TAZ-mediated control over cGAS-STING signalling and senescence stands a previously underappreciated role of YAP/TAZ at preserving the structural and functional integrity of the NE. We next aimed to understand the molecular basis of this event. As YAP/TAZ are transcriptional coactivators, we searched for YAP/TAZ target genes encoding for candidate proteins able to sustain NE integrity. We thus parsed the WI-38 RNA-seq dataset searching for YAP/TAZ -controlled genes encoding for cytoskeletal and nuclear lamina proteins. Candidate factors were validated as *bona fide* YAP/TAZ targets by RT-qPCR, obtaining a final list of 9 proteins (see Supplementary Table 3). Our attention was first attracted by an obvious candidate: lamin B1, a structural component of the nuclear lamina, required for NE integrity[35]. lamin B1 expression has been shown to decline in senescent cells in vitro[36], and also during ageing in distinct tissues[37,38], at least in part through unknown upstream transcriptional mechanisms[36]. As shown in Extended Data Fig. 10h, YAP/TAZ are required for lamin B1 mRNA and protein expression. Consistently with previous results[23,24,39], silencing of lamin B1 with independent siRNA pairs led to the upregulation of *CXCL10* and other SASP markers, in a cGAS-dependent manner (Extended Data Fig. 10i, j). That said, the effects of lamin B1 inactivation on SASP induction were minor compared to the effect of YAP/TAZ inactivation, indicating the existence of additional downstream effectors of YAP/TAZ for these responses (Extended Data Fig. 10j).

To search for such factors, we carried out a functional screen, whereby each of the previously validated YAP/TAZ targets was knocked down by independent siRNAs and assayed for *CXCL10* upregulation (Supplementary Table 3). The screen returned only one hit: *ACTR2*, encoding for ARP2, a core component of the ARP2/3 complex involved in actin filament nucleation[40]. mRNA levels of *LMNB1* and *ACTR2* were also attenuated after YAP/TAZ inhibition (Extended Data Fig. 10k). Given the role of YAP/TAZ at preserving the peri-nuclear actin cap, we next investigated whether ACTR2 is required to preserve this structure and, if so, control nuclear shape. Attenuation of ACTR2 in fibroblasts caused complete disappearance of the actin cap (Fig. 5e, left panels and Extended Data Fig. 10l); this effect not only preceded, but was quantitatively far more pronounced and pervasive than any effect of ACTR2 downregulation on focal adhesions (Extended Data Fig. 10m), indicating that a high dosage of ACTR2 is essential for actin cap formation but not for focal adhesions. As consequence of loss of the actin cap, the nucleus bulged and wrinkled, and this was paralleled by cGAS nuclear accrual and activation of cGAMP (Fig. 5e and Extended Data Fig. 10n). Moreover, ACTR2 knockdown induced SASP genes in a cGAS- and STING-dependent manner (Fig. 5f and Extended Data Fig. 10o), and concomitant ACTR2 and lamin B1 loss approximated the effects of YAP/TAZ depletion (Fig. 5g).

To reinforce the notion that building an actin cap is a crucial determinant of YAP/TAZ-regulated NE integrity, we asked whether the effects of YAP/TAZ inactivation might be rescued by experimentally supporting ARP2/3 function. Indeed, residual ARP2/3 remains in YAP/TAZ depleted cells (Extended Data Fig. 10k), as also implied by the presence of other F-actin structures, such as stress fibers and transverse arcs. To boost ARP2/3 function, we considered the depletion of arpin, a natural inhibitory factor of ARP2/3-driven actin nucleation[41]. Indeed, arpin knockdown rescued the effects of YAP/TAZ inactivation on perinuclear actin cap, nuclear morphology, cGAS activation and induction of SASP (Fig. 5e, h and Extended Data Fig. 10r). We conclude from this collective set of experiments that YAP/TAZ control NE integrity through a dual and partially redundant mechanism: by supporting lamin B1 expression and by inducing the formation of the ACTR2-controlled actin cap.

Similar to YAP/TAZ depletion, YAP/TAZ functional attenuation by low mechanical strains decreased expression of ACTR2 and laminB1, and caused loss of actin cap, nuclear dysmorphia and SASP induction (Extended Data Fig. 11a-d), consistent with mechanical regulation of cGAS (as in Extended Data Fig. 6). These responses were rescued by experimentally sustaining YAP activity (Extended Data Fig. 11a,c,d). Of note, the regulation of LaminB1 and ACTR2 mRNA expression by YAP/TAZ occurs also independently from cell proliferation (Extended Data Fig. 11a).

Next, we asked whether *LMNB1* and *ACTR2* are direct targets of YAP/TAZ. YAP/TAZ control transcription from promoters or, more frequently, from enhancers located distantly from the transcription start site (TSS) of the gene they regulate[27]. We thus queried the YAP/TAZ chromatin ‘interactome map’, listing YAP/TAZ-bound *cis*-regulatory elements, including enhancers physically interacting with TSS by chromatin looping[42]. YAP/TAZ is predicted to bind to the LMNB1 promoter and to enhancers connected to the promoter of ACTR2 (Extended Data Figure 11e). Crucially, we experimentally validated that YAP/TAZ were specifically bound to these chromatin regions by chromatin immunoprecipitation-qPCR (ChIP-qPCR) suggesting that *LMNB1* and *ACTR2* are direct YAP/TAZ target genes in both fibroblasts and vSMCs (Fig. 5i and Extended Data Fig. 11f, g).

Discussion

Here we identified a molecular mechanism regulating in vivo cell senescence and ageing centered on the YAP/TAZ-cGAS-STING signalling conduit, revealing an unexpected link between mechanosensing and innate immunity. We perceive distinct elements for discussion. To start, we show that physiological ageing of multiple tissues parallels declining mechanotransduction, as visualized by attenuated YAP/TAZ activity and reduced cellular mechanosignalling. Future work will be required to further dissect the intimate causes underlying changes in mechanotransduction during ageing; these may be due, for example, to alterations in the physical properties of the ECM, in the viscoelastic properties of the whole tissue, in integrin-ECM association, or linked to more cell intrinsic alterations, such as defective contractility, or other changes. Irrespectively, here we show that mimicking such natural decline through experimental YAP/TAZ inactivation leads to in vivo accrual of senescent cells and accelerated emergence of age-related tissue degenerations. Conversely, sustaining YAP/TAZ can block these processes in vitro and in vivo.

The findings break new ground on the nature of the signals and mechanisms inducing senescence in vivo. Depletion of senescent cells by senolytics has been shown to ameliorate ageing traits as such connecting accumulation of senescent cells to ageing[1,2]. Yet, the upstream molecular events that induce senescence in living tissues have so far remained unclear. These unknowns can be addressed, at least in part, by the present discovery of the YAP/TAZ-cGAS-STING connection, envisioning a seesaw where elevated activities of YAP/TAZ in young cells keep cGAS-STING at bay, whereas unscheduled cGAS-STING activation occurs as consequence of reduced YAP/TAZ activity. It's worth noting that, in the cellular models here adopted, cGAS-STING mediate a substantial fraction of YAP/TAZ transcriptional responses, implicating a leading role of YAP/TAZ as regulator of cGAS-STING in stromal cells. Our data at least suggest that when youthful YAP/TAZ mechanotransduction is eroded, a number of cGAS-inducing inputs may go unchecked. This may be caused by excessive shuttling of nucleases in the nucleus[43], mitochondrial stress, loss of heterochromatin and other genetic or acquired mechanisms[26]. Intriguingly, the latter include mechanical strain themselves, damaging the nucleus above its point of resilience[44–46]. While the nature of such damaging mechanisms remains unknown, we can only speculate at this stage that mechanical activation of YAP/TAZ and its NE-protecting effects may contribute to a feedback that imbues mechanical resilience.

The identity of the cell types initiating senescence in living tissues remains poorly investigated. Here we found that waning levels of YAP/TAZ mechanotransduction is not a generalized feature of all cell types but occurs primarily in stromal and contractile cells. It is in these same cell types that we validated the YAP/TAZ-cGAS-STING connection to senescence and ageing-related tissue dysfunctions; it is thus tempting to propose that ageing may primarily initiate in tissues providing the structural framework and mechanical support to mammalian organs.

Another element of interest relates to the unexpected role of YAP/TAZ as protectors of the nuclear envelope. We identified two direct YAP/TAZ targets as mediators of this effect: laminB1, for which a role in ageing and senescence has been already proposed[23,24,36–39] but for which here we found only a partial role in preventing senescence when compared to YAP/TAZ; and ACTR2, an F-actin modulator that we found essential for the formation of the actin cap, a cytoskeletal structure intimately associated to the NE[31], preventing nuclear aberrations and fragility with ensuing cGAS activation and senescence.

In vitro studies on different cell types already suggested either positive or negative roles of YAP/TAZ in regulating the expression of distinct senescence markers[21,47,48]. Irrespectively, the endogenous function of YAP/TAZ as regulator of senescence in adult tissues in vivo, and in specific cell types, remained unexplored, let alone the role of YAP/TAZ in ageing. The present results establish YAP/TAZ as factors playing physiological functions in youthful tissue homeostasis. This represents a departure from the current view of YAP/TAZ as relevant for cancer and tissue regeneration but irrelevant for normal adult homeostasis, as inferred by the inconsequentiality of YAP/TAZ genetic ablation in many epithelial tissues[49].

As for cGAS-STING, the central role of this cascade for inducing cell senescence is well-established in vitro[23–25]. However, the in vivo role of aberrant cGAS-STING signalling as inducer of functional decline and ageing-related dysfunctions, as consequence of its pro-senescence properties, remains undefined[26]. Our work contributes to fill this gap by showing that STING inhibition in vivo is sufficient to prevent accrual of senescent cells and, in so doing, the later emergence of accelerated ageing traits. Previous work had connected YAP/TAZ nuclear entry to nuclear pore stretching, linking nuclear mechanics and YAP/TAZ mechanotransduction[34]. Here we offer a complementary perspective, wherein YAP/TAZ activity is in turn instrumental to preserve the mechanical resilience of the nuclear envelope. This raises the possibility of mechanically regulated feedback loops between YAP/TAZ and the physical attributes of the nucleus and the cytoskeleton to be explored in future work, and particularly in the context of ageing biology.

We believe that the mouse models here generated represent new tools for the study of ageing induced by accrual of senescent cells, allowing to capture events that are normally rare (occurring over years during physiological ageing), and starting in specific cell types and in a time-controlled manner. In perspective, this may incite investigations on the cell-autonomous and non-cell autonomous mechanisms of ageing with unprecedented depth and spatiotemporal resolution. This breaks new ground over models so far used as workhorses in ageing research such as progeroid-like syndromes associated to DNA repair factors and lamin deficiencies[50]. Irrespectively, we note that induction of senescence represents a common trait of most of these models[50]; as such, the present demonstration of STING inhibition as means to ameliorate ageing-related tissue degenerations in YAP/TAZ cKO mice suggests the possibility of broader applications, whereby STING inhibition may represent a valid alternative to current senolytics approaches, aiming to preserve tissue integrity by preventing senescence rather than eliminating cells. Moreover, since ageing integrates several comorbidities in distinct organs, our work on the YAP/TAZ and cGAS-STING connection warrants further explorations in other cell types in which YAP/TAZ declines during ageing, and whose senescence may initiate other ageing-related pathologies.

Materials & Methods

Mouse experiments

Animal experiments were performed adhering to our institutional guidelines as approved by the OPBA (University of Padua) and the Ministry of Health of Italy. The housing conditions comprised a diet with 28% protein. A maximum of five adult mice weighing up to 20 g were homed in a single cage, maintaining the ambient temperature at 19–23°C, the humidity at 55%±10% and a 12-hour light/12-hour dark cycle. For all studies employing the *Smmhc-CreER*^{T2} driver and accompanying studies involving the aortic wall, only male mice were considered, as this allele is harbored on the Y-chromosome. Male and female mice were equally included in all the other studies. Well-being of experimental animals was monitored by a licensed veterinary and mice were sacrificed as per veterinary advice as soon as they started to manifest signs of suffering, including lethargy, abdominal fluid accumulation and other manifestations of poor health.

Transgenic lines were kindly provided by: D. Pan (*Yap1*$^{fl/fl}$[52]), F. Camargo (*tetO-YAPS127A*[16]), G. M. Bressan (*Smmhc-CreER*^{T2}[17] and *Fbn1*$^{C1039G/WT}$[53]. Double *Yap*$^{fl/fl}$*; Taz (Wwtr1)*$^{fl/fl}$ conditional knockout mice were as previously described[54]. *R26-rtTAM2* (Stock No: 006965), *Col1a2-CreER* (Stock No: 029235), *R26-LSL-rtTA* (Stock No: 005670), *R26-LSL-LacZ* (Stock No: 003309), and *Sting*$^{Gt/Gt}$ (Stock No: 017537) transgenic mice were from Jackson Laboratory. *R26-CAG-CreER; Yap*$^{fl/fl}$*; Taz*$^{fl/fl}$ mice were generated as previously described[55]. To selectively ablate *Yap/Taz* in fibroblasts of adult mice, mice carrying *Yap*$^{fl/fl}$*; Taz*$^{fl/fl}$ conditional alleles were bred with *Col1a2-CreER* transgenic mice to obtain *Col1a2-CreER; Yap*$^{fl/fl}$*; Taz*$^{fl/fl}$ mice. Conditional ablation of the floxed *YAP/TAZ* alleles was triggered by treating 2.5-month-old *Col1a2-CreER; Yap*$^{fl/fl}$*; Taz*$^{fl/fl}$ mice with one oral gavage of Tamoxifen (0.11 mg g^{-1} body weight) per day, during 2 consecutive days, every week for the duration of the experiment. Tamoxifen was dissolved in corn oil. Controls were *Yap*$^{fl/fl}$*; Taz*$^{fl/fl}$ mice treated with the same regime.

To selectively ablate *Yap/Taz* in vascular smooth muscle cells of adult mice, mice carrying *Yap fl/fl; Taz fl/fl* conditional alleles were bred with *Smmhc-CreER*^{T2} transgenic mice to obtain *Smmhc-CreER*^{T2}*; Yap fl/fl; Taz fl/fl* mice. Conditional ablation of *YAP/TAZ* floxed alleles in smooth muscle cells of adult mice was triggered by treating 2.5-month-old *Smmhc-CreER*^{T2}*; Yap fl/fl; Taz fl/fl* mice with one oral gavage of 6.6 mg Tamoxifen per day, for 5 consecutive days. Controls were *Smmhc-CreER*^{T2} mice treated with the same regime. The same protocol was applied for activation of rtTA expression in *Smmhc-CreER*^{T2}*; R26-LSL-rtTA* combinations (see below).

Under veterinary advice, YAP/TAZ cKO mice were sacrificed when started to show sign of suffering, including lethargy, abdominal fluid accumulation and other signs of poor health.

For Sting inactivation-related studies, *Col1a2-CreER; Yap fl/fl; Taz fl/fl* mice or *Smmhc-CreER*^{T2}*; Yap fl/fl; Taz fl/fl* mice were crossed to *Sting Gt/Gt* mice to obtain *Col1a2-CreER; Yap fl/fl; Taz fl/fl; Sting Gt/Gt* or *Smmhc-CreER*^{T2}*; Yap fl/fl; Taz fl/fl; Sting Gt/Gt* mice, respectively. For pharmacological inhibition of Sting, Tamoxifen-treated (as detailed above) *Smmhc-CreER*^{T2}*; Yap fl/fl; Taz fl/fl* mice were injected intraperitoneally with 600 nmol C-176 (Sigma-Aldrich) in corn oil (Sigma-Aldrich), daily, for the duration of the experiment. Controls were *Smmhc-CreER*^{T2}*; Yap fl/fl; Taz fl/fl* mice treated with vehicle. C-176 treatment started 5 days prior to the initiation of Tamoxifen treatment.

For YAP overexpression studies, *Col-tetO-YAPS127A* mice were crossed with either *R26-rtTAM2* or *Smmhc-CreER*^{T2}*; Fbn1*$^{C1039G/WT}$*; R26-LSL-rtTA* mice to obtain *R26-rtTAM2; Col-tetO-YAPS127A* or *Smmhc-CreER*^{T2}*; Fbn1*$^{C1039G/WT}$*; R26-LSL-rtTA; Col-tetO-YAPS127A* mice, respectively. To experimentally sustain YAP activity in adult fibroblasts in vivo, 3-month-old *R26-rtTAM2*; *Col-t etO-YAPS127A* mice were subjected to a cyclic treatment (2 days administration followed by 5 days of withdrawal) of 0.5 mg/ml doxycycline (Sigma-Aldrich) in drinking water, every week for the duration of the experiment; controls were *Col-tetO-YAPS127A* mice (i.e., lacking *R26-rtTAM2*) treated with the same regimen. To experimentally sustain YAP activity in smooth muscle cells of adult *Fbn1*$^{C1039G/WT}$ mice, 5-month-old *Fbn1*$^{C1039G/WT}$*; Smmhc-CreER*^{T2}*; R26-LSL-rtTA; Col-tetO-YAPS127A* mice (pre-treated with Tamoxifen as above) were treated with 2 mg/ml doxycycline in drinking water, for five consecutive days a week, every week for the duration of the experiment (till 7 months of age). Controls were Marfan mice, or Marfan mice having any incomplete genotype, treated with the same regimen and showing no effect.

To evaluate the specificity of the *Smmhc-CreER*^{T2} driver, *Smmhc-CreER*^{T2}*; R26-LSL-LacZ* mice were treated with one oral gavage of 6.6 mg Tamoxifen per day, for 5 consecutive days. Mice were sacrificed and analyzed for LacZ expression one week after the completion of the treatment. Animals were genotyped with standard procedures[56] and with the recommended set of primers.

Histological examination

For organ collection, mice were euthanized by cervical dislocation and perfused with PBS. Unless otherwise specified, organs were freshly collected, fixed in 4% PFA (Sigma-Aldrich) in PBS overnight and processed for paraffin embedding, H&E staining and histological analysis. Aorta was freshly excised, embedded in OCT tissue-freezing medium (Sigma-Aldrich), frozen in the vapor phase of liquid nitrogen and sectioned at 2.5-μm thickness for histological analysis. Histological quantifications were performed using ImageJ software (version 2.0.0-rc-69/1.52i). Collagen visualization on tissue sections was carried out by Picrosirius Red staining, as previously described[57]. Collagen birefringence images were acquired with a Leica 5000B microscope under orthogonal polarized light.

Periodic acid–Schiff (PAS) staining on kidney sections was performed as follows: sections were deparaffinized and rehydrated, oxidized in 0.5% periodic acid solution for 5 minutes, rinsed in distilled water and placed in Schiff reagent (Sigma-Aldrich) for 30 minutes. Samples were then washed in lukewarm tap water and counterstained in hematoxylin for 5 minutes, washed in tap water, dehydrated and mounted in mounting medium.

Elastic fiber staining on aortic sections was carried out as follow: sections were fixed in 4% PFA in PBS for 10 minutes, incubated in 70% Ethanol for 5 minutes and stained in Verhoeff’s stain for 1 hour. Verhoeff’s stain was freshly prepared by mixing 20 ml of 5% hematoxylin in ethanol, 8 ml of 10% ferric chloride in distilled water and 8 ml of Weigert’s iodine solution (2 g of potassium iodide and 1 g of iodine in 100 ml of distilled water). For the differentiation of the staining, slides were rinsed in tap water, then placed in 2% ferric chloride for 1-2 minutes. Differentiation was stopped in tap water when elastic fibers appeared black on a grey background. Sections were treated with 5% sodium thiosulfate for 1 minute, washed in tap water for 5 minutes and dehydrated through 95% ethanol and 100% ethanol. Slides were cleared twice in xylene for 3 minutes and mounted in mounting medium.

Activity of LacZ in aortic sections was detected by X-GAL staining using the β-Galactosidase Reporter Gene Staining Kit (Sigma-Aldrich), according to the manufacturer’s instructions.

Immunofluorescence and immunohistochemical staining

Immunofluorescence on PFA-fixed cells, on PFA-fixed paraffin-embedded tissue slices and on OCT(Sigma-Aldrich)-embedded tissue slices was performed as previously described[57]. Samples were counterstained with ProLong-DAPI (Termo Fisher Scientific, P36971). Confocal images were acquired on a Leica STELLARIS 5 microscope, using LASX software (version 4.1.0.23081). Superresolution images were obtained with the LIGHTNING module. 3D reconstructions were obtained from Z-stacks using the LASX software. All images were analyzed using ImageJ software (version 2.0.0-rc-69/1.52i). Primary and secondary antibodies used for the immunofluorescence staining are listed in Supplementary Table 4. YAP/TAZ, p-MLC2, p-FAK, cGAS and F-Actin immunofluorescence stainings were performed on OCT-embedded tissue slices. Elastic lamellae autofluorescence was detected upon excitation with the 488 laser line.

Immunohistochemical staining was performed on PFA-fixed, paraffin-embedded tissue sections as previously described[57]. Brightfield images were obtained with a Nanozoomer Scanner 2.0RS (Hamamatsu), equipped with the NDPscan3.1 software. Primary antibodies used in immunostaining are listed in Supplementary Table 4.

Quantifications from immunofluorescence and immunohistochemistry staining were performed using ImageJ software (version 2.0.0-rc-69/1.52i).

In situ hybridization

PFA-fixed cells and PFA-fixed, paraffin-embedded skin and kidney sections and OCT-embedded aortic sections were processed for RNA *in situ* detection using the chromogenic RNAscope 2.5 HD Duplex Detection Kit (Advanced Cell Diagnostics), according to the manufacturer’s instructions, using probes detected by the Fast Red (Advanced Cell Diagnostics, REF 320459) or the Fast Green (Advanced Cell Diagnostics, REF 320719) detection reagents. Mouse RNAscope probes detected using the Fast Red detection reagent were: Mm-*Cdkn1a* (Cat. Number 408551-C2), Mm-*Il1β* (Cat. Number 316891-C2). Mouse RNAscope probes detected using the Fast Green detection reagent were: Mm-*Cxcl10* (Cat. Number 408921), Mm-*Mmp3* (Cat. Number 480961), CRE (Cat. Number 312281). Human RNAscope probe detected using the Fast Red detection reagent was: Hs-*CXCL10* (Cat. Number 311851-C2). Tissue section nuclei were counterstained with 1:1 v./v distilled water/Gill No. 1 Hematoxylin solution (Sigma-Aldrich, GHS132) and slides were mounted with the VectaMount™ Permanent Mounting Medium (VECTOR Laboratories, LS-J1037). Brightfield images were acquired with a NanoZoomer 2-ORS scanner (Hamamatsu), equipped with the NDPscan3.1 software. Cell nuclei were counterstained with ProLong-DAPI (Termo Fisher Scientific, P36971) and slides were mounted with the VectaMount™ Permanent Mounting Medium (VECTOR Laboratories, LS-J1037). Confocal images were acquired on a Leica STELLARIS 5 microscope, using LASX software (version 4.1.0.23081). *CXCL10* probe autofluorescence was detected upon excitation with the 550 laser line.

In situ Proximity Ligation Assay

Proximity ligation assay (PLA) was performed using Duolink PLA kit (Sigma Aldrich) according to the manufacturer’s protocol using the following primary antibodies: anti-cGAS (clone D1D3G, #15102, 1:100 pH9, Cell Signaling) and anti-DNA double stranded (clone

AE-2, MAB1293, 1:100 pH9, Abcam). Negative controls were performed using only one primary antibody.

Slides were analyzed under a Zeiss Axioscope A1 and microphotographs were collected using a Zeiss Axiocam 503 Color with the Zen 2.0 Software (Zeiss).

Single-cell RNA seq

Yap fl/fl; Taz fl/fl (Control) and *Col1a2-CreER; Yap fl/fl; Taz fl/fl* (Y/T cKO) mice were treated with Tamoxifen (as described above) and euthanized after 4 weeks. 24-month-old wild-type mice (Old) served as reference for natural aging. To obtain a single cell suspension, mouse dorsal skin was incubated (after fur removal) in Collagenase, Type I (2000U/ml in PBS - Thermo Fisher Scientific, CAS No. 9001-12-1) for 1 hour at 37°C with gentle agitation. Cells were then washed in PBS and filtered repeatedly through a 70 μm cell strainer to remove cell debris and ECM contaminants.

Droplet-based single cell RNA-capture was performed with the Chromium Single Cell 3’ kit v3.1 (10x Genomics). Cell concentration was determined with an automated cell counter and the adequate volume of cellular suspensions were loaded on a Chromium Controller to generate single-cell gel bead emulsions, targeting 10,000 cells. cDNA generation and library preparation were performed according to manufacturer’s instructions. Libraries were sequenced to an average depth of 50,000 reads per cell on an Illumina Novaseq 6000 system.

The Cell Ranger Count pipeline (version 3.1.0) was used to align reads to the mouse reference transcriptome (mm10) and to calculate UMI counts from the mapped reads.

Expression data were imported in R and analyzed using Seurat R package (version 3.1.5[58]). Low quality and multiplet cells were identified as outliers within the distribution of the number of genes, UMI counts, and percent of reads mapping on mitochondrial genes per cell (see Supplementary Table 5 for details), and subsequently discarded. Specifically, cell multiplets were defined using Scrublets (v. 0.2.1[59]) in python3.6. We finally retained a total of 9579, 6289 and 5414 cells for Control, Y/T cKO and Old samples, respectively.

Clusters representing fibroblasts were identified using singleR (v. 1.0.6[60]) with the ImmGen reference set and visually verified using the expression level of *Vimentin* and *Pdgfra*. Fibroblast transcriptomes from the different conditions were compared using the *FindMarkers* function of the Seurat package with default parameters. Differentially expressed genes (LognFC ≥ 0.25; Bonferroni-adjusted p-value ≤0.05) were annotated for Biological Process gene ontologies using the Enrichr website (https://maayanlab.cloud/Enrichr/).

The Cordenonsi YAP conserved signature[9] has been obtained from the Molecular Signature Database (https://www.gsea-msigdb.org/gsea/msigdb/index.jsp) and converted to mouse homologous genes using the HUGO Gene Nomenclature Committee (HGNC) database (https://www.genenames.org/cgi-bin/hcop). Average signature expression has been calculated as the average expression of all signature genes in all cells.

Single cell transcriptomic data from *Tabula Muris Senis* and mouse skeletal stem cells (SSCs)

The single cell RNA-seq data of the *Tabula Muris Senis* atlas[10] has been obtained from Gene Expression Omnibus GSE149590. Briefly, we downloaded 10X genomics single-cell raw counts and cell annotations from the H5AD object file of GSM4505404, and normalized the raw data using the functions of the *Seurat* R package (version 3.1.5[58]). Gene expression values have been extracted from cells of young and aged mice subgroups of kidney (fibroblasts, distal convoluted tubule epithelial cells and Henle's loop epithelial cells at 1 and 3 months for young, and at 24 and 30 months for old), heart and aorta (fibroblasts of cardiac tissue, cardiomyocytes and leukocytes at 1 and 3 months for young, and at 21 and 24 months for old), limb muscle (mesenchymal stem cells, smooth muscle cells and Schwann cells at 1 and 3 months for young, and at 24 and 30 months for old), lung (ciliated and club cells of the bronchioli at 1 and 3 months for young, and at 21 and 30 months for old), mammary gland (basal and luminal epithelial cells at 3 months for young, and at 21 months for old), liver (hepatocytes at 1 and 3 months for young, and at 21, 24 and 30 months for old) and brain (interneurons at 3 months for young, and at 24 months for old).

Raw single cell RNA-seq data of mouse skeletal stem cells[60] has been downloaded from Gene Expression Omnibus GSE161946. Raw counts have been processed according to the Processing Notebook pipeline (available at GSE161946 as Supplementary file) to generate normalized gene expression values for 302 cells; SSCs from mice of 2 (young) and 24 (old) months were used for the subsequent analyses.

YAP/TAZ activity has been calculated using the "Cordenonsi YAP conserved signature" for all cell types but cardiomyocytes, for which we used a list of cardiomyocyte-specific YAP direct target genes identified by ChIP-seq in the mouse heart[61]. Average signature expression has been calculated as the average expression of all signature genes in the cell subgroups.

Reagents and Plasmids

Fetal bovine serum (10270-106), L-glutamine (25030-024), Pen/Strep (15140-122), DMEM/F12 (11320-074), DMEM (41965-039), MEM (31095-029), trypsin-EDTA 0.05% (25300-054), CK-869 (C9124)[62], H-151 (SML2437), Palbociclib (PZ0383), Remodelin (5.31066) and 2',3' dideoxycytidine (D5782) were from Sigma-Aldrich. Pyrintegrin (HY-13306) was from MedChemExpress. C3 (#CT04) was from Cytoskeleton Inc. Human smooth muscle cell growth medium 2 was from PromoCell (C-22062).

The pCW57.1-YAP5SA vector was generated by subcloning YAP5SA into the pCW57.1 vector (Addgene #41393). pTRIP-EF1a-EGFP-Flag-Cgas E225A-D227A was cloned by substituting the CMV promoter of pTRIP-CMV-EGFP-Flag-Cgas E225A-D227A vector (AddGene #86674) with the EF1a promoter from the MXS_EF1a vector (AddGene #62421) via MluI/SalI enzymatic digestion.

The EGFP-KASH2 vector was cloned by amplifying the KASH domain of the SYNE2 (Nesprin2) gene from human cDNA, using

KASH Forward

AAGGGTAGCGGCAGCGGTGGTAGCGGTCAGCTGAACTCTGATATCAGCGCC and KASH Reverse

CAGCTGACCGCTACCACCGCTGCCGCTACCCTTGTACAGCTCGTCCATGCC primers.

This KASH amplicon was then fused in frame to an EGFP PCR product isolated from AddGene #64060 plasmid, using

EGFP Forward

AATGAATTCGCCGCCACCATGGTGAGCAAGGGCGAGGAG and EGFP Reverse

CAGCTGACCGCTACCACCGCTGCCGCTACCCTTGTACAGCTCGTCCATGCC primers.

The resulting EGFP-KASH2 fusion PCR product was subcloned into the pCW57.1 vector (Addgene #41393) via EcoRI/SalI enzymatic digestion after the introduction of a suitable multiple cloning site.

All constructs were confirmed by sequencing.

Cell lines, treatments and transfections

Primary mouse adult fibroblasts (MAFs) were isolated from biopsies of dorsal skin. Briefly, tissue was minced and digested in Collagenase, Type I (2000 U/ml in PBS - Thermo Fisher Scientific, CAS No. 9001-12-1) for 1 hour at 37°C, with vigorous shaking. Samples were filtered through a 70 μm cell strainer, plated on 0.2% gelatin-coated dish and maintained in DMEM-F12 medium, supplemented with 20% Fetal Bovine Serum (FBS), L-Glutamine and antibiotics.

Primary mouse adult smooth muscle cells were isolated from freshly explanted aortae. Briefly, tissue was digested in enzyme solution (Collagenase Type II 1mg/ml, Elastase 0.7 U/ml, Soybean Trypsin inhibitor 1 mg/ml in HBSS) for 10 minutes at 37°C. After adventitia and endothelial cell layer removal, tissue was incubated in enzyme solution for 40 minutes at 37°C. Cells were plated on collagen I-coated (1:50 diluted in 0.02 M Acetic Acid) dish and maintained in DMEM-F12 medium, supplemented with 20% Fetal Bovine Serum (FBS), L-Glutamine and antibiotics. Upon the first passage, cells were maintained in DMEM-F12 medium, supplemented with 5% Fetal Bovine Serum (FBS), L-Glutamine and antibiotics.

WI-38 human fibroblasts were from ECACC (Cat. Number 90020107) and maintained in MEM medium, supplemented with 10% Fetal Bovine Serum (FBS), L-Glutamine and antibiotics.

Human aortic smooth muscle cells were from PromoCell (C12533) and maintained in human smooth muscle cell growth medium 2.

HEK293T cells were from ATCC and maintained in DMEM medium, supplemented with 10% Fetal Bovine Serum (FBS), L-Glutamine and antibiotics. HEK293T cells were authenticated by DSMZ/Eurofins Genomics.

All cell lines were routinely tested for mycoplasma contamination and confirmed negative.

For *ex vivo Yap/Taz* depletion studies, primary dermal fibroblasts (MAFs) isolated from *R26- CAG- CreER; Yap fl/fl; Taz fl/fl* mice were treated with 1 µM 4OH-Tamoxifen (Sigma-Aldrich) for 72 hours. Control cells were MAFs isolated from *Yap fl/fl; Taz fl/fl* mice, also treated with 1 µM 4OH-Tamoxifen. For *ex vivo* YAP overexpression studies in primary fibroblasts, MAFs isolated from *R26-rtTAM2; Col-tetO YAPS127A* mice were treated with 10 µg/ml doxycycline hyclate (Sigma-Aldrich) for the duration of the experiment.

Lentiviral particles preparation and cell culture infection were performed as previously described[63], with modifications. Briefly, cells were brought to single-cell suspension, overlaid with viral supernatant and spun at 7.0 RCF for 1.5 hours. For *in vitro* YAP overexpression studies in WI-38 fibroblasts, cells were transduced with the lentiviral pCW57.1-YAP5SA vector (or empty pCW57.1 vector as control) and maintained in the presence of 10 µg/ml doxycycline hyclate (Sigma-Aldrich) for 36 hours. For EGFP-cGAS reporter studies on primary MAFs and WI-38 fibroblasts, cells were transduced with the lentiviral pTRIP-EF1a-EGFP-Flag-Cgas E225A-D227A vector.

siRNA transfection in WI-38 fibroblasts was carried out using Lipofectamine RNAi-MAX (Life Technologies, 56532) in antibiotics-free medium, according to the manufacturer’s instructions. siRNA transfection in primary MAFs and primary mSMC was carried out using GenMute siRNA transfection reagents (SignaGen Laboratories, SL100568-SMC), according to the manufacturer’s instructions. Cells were harvested 48 hours after siRNA transfection, unless otherwise specified.

Sequences of human and murine siRNAs are listed in Supplementary Table 6. The negative control siRNA (siCo) was from Qiagen (AllStars Negative Control siRNA, 1027281).

For in vitro pharmacologic treatments, controls were treated with the same volume of the appropriate vehicle (DMSO for Pyrintegrin, CK-869 and Remodelin; ethanol for H-151 and 4OH-tamoxifen; water for Rho inhibitor C3 and 2’,3’-dideoxycytidine).

Gene expression analyses by RNA-seq

Cells were harvested by the RNeasy Mini Kit (Qiagen - 74106) or the NucleoSpin 8 RNA Core Kit (Macherey-Nagel - 740465.4) for total RNA extraction and contaminant DNA was removed with rDNase Set (Macherey-Nagel, 740963) or RNase-Free DNase Set (Qiagen – 79254).

RNA-seq libraries for deep-sequencing were prepared with QuantSeq 3’mRNA-Seq Library Prep kit (LEXOGEN), and sequencing was performed with NextSeq500 System (Ilumina). About 20M reads per sample were obtained. Read quality was verified using fastQC (version 0.11.3; http://www.bioinformatics.babraham.ac.uk/projects/fastqc/). Raw reads were trimmed for adapters, polyA read through, and low-quality tails (quality <Q20) using BBDuk (version 37.02; sourceforge.net/projects/bbmap/). Reads shorter than 35 bp were also removed resulting on average 27 M trimmed reads per sample. Reads were subsequently aligned to the human reference genome (hg38) for human fibroblasts, or to the mouse reference genome (mm10) for mouse fibroblasts, using STAR (version 2.5.3a[64]) and setting the STAR parameters as indicated in the Lexogen data analysis guidelines (see https://www.lexogen.com/quantseq-data-analysis/ for details). Raw gene counts were obtained using the *featureCounts* function of the *Rsubread* R package (version 1.30.3[65]) and the Gencode gene annotation for hg38 genome for human fibroblasts or for mm10 genome for mouse fibroblasts. Gene counts were normalized to counts per million mapped reads (CPM) using the *edgeR* package[66]; only genes with a CPM greater than 1 in at least 2 samples were further retained for differential analysis. Differential gene expression analysis was performed using the *exactTest* function of the *edgeR* package[66]. Genes were considered significantly differently expressed at False Discovery Rate (FDR) ≤0.05 and absolute fold-change ≥1.5.

Results from the analysis of differential expression were functionally annotated using Gene Set Enrichment Analysis (GSEA) software[67] (http://software.broadinstitute.org/gsea/index.jsp) in preranked mode to the gene list ranked on log2 fold change to evaluate the enrichment for gene signatures. Gene signature were the Hallmark gene sets, derived from the Molecular Signature database at the GSEA website (https://www.gsea-msigdb.org/gsea/msigdb/index.jsp) and previously published gene signatures[68–75]. Gene sets were considered significantly enriched at FDR ≤ 0.05 when using classic enrichment statistics and 1,000 permutations of gene sets.

Western Blot

Tissues were mechanically homogenized using a pellet pestle motor in lysis buffer (20 mM HEPES (pH 7.8), 100 mM NaCl, 5% glycerol, 0.5% NP-40, 5 mM EDTA, 1 mM dithiothreitol, and phosphatase and protease inhibitors), lysed by ultrasound sonication (Diagenode Bioruptor) and centrifuged for 10 min at 4°C. Total protein content was determined by Bradford quantification. Western blot analysis was performed as previously described[76]. GAPDH or αTUBULIN served as loading controls. Images were acquired with Image Quant LAS 4000 (GE healthcare). The list of antibodies used in this study and the corresponding dilutions are provided in Supplementary Table 4.

Cytokine profiler array

To obtain conditioned medium from YAP/TAZ KO MAFs, *Yap fl/fl; Taz fl/fl* and *R26-CAG-CreER; Yap fl/fl; Taz fl/fl* MAFs were cultured for 72 hours in serum-free medium (Opti-MEM – Gibco 51985-026) in the presence of 1 μM 4OH-Tamoxifen (Sigma-Aldrich, T176). Primary mSMC were transfected with the appropriate siRNA (as detailed above), and cultured in serum-free medium (Opti-MEM – Gibco 51985-026) for 48 hours. Conditioned medium was then collected and cytokines detection was performed using the Proteome Profiler Mouse XL Cytokines Array (R&D - ARY028) for MAFs and using the Proteome Profiler Mouse Cytokine Array Kit, Panel A (R&D, ARY006) for mSMC, according to the manufacturer’s instructions. Intensity values were extracted using ImageJ. For each value, the local background intensity was subtracted and each array was normalized to the intensity of the internal positive control.

cGAMP ELISA

Yap fl/fl; Taz fl/fl and *R26-CAG-CreER; Yap fl/fl; Taz fl/fl* MAFs were cultured for 72 hours in the presence of 1 µM 4OH-Tamoxifen (Sigma-Aldrich, T176). Primary mSMC were transfected with siRNA against YAP/TAZ, with or without the concomitant depletion of cGAS, and cultured for 48 hours. Cells were harvested in Lysis Buffer (20 mM HEPES (pH 7.8), 100 mM NaCl, 5% glycerol, 0.5% NP-40, 5 mM EDTA, 1 mM dithiothreitol and phosphatase and protease inhibitors) and lysed by sonication. 2’-3’-cGAMP levels in cell lysates were detected using the 2’3’-cGAMP ELISA Kit (Cayman Chemicals - 501700), according to the manufacturer’s instructions.

WI-38 were transfected with siRNA against ACTR2, with or without the concomitant depletion of cGAS, and cultured for 48 hours. Cells were harvested in Lysis Buffer and lysed by sonication. 2’-3’-cGAMP levels in cell lysates were detected using the 2’3’-cGAMP Competitive ELISA Kit (Thermo Fisher Scientific - EIAGAMP), according to the manufacturer’s instructions.

RT-qPCR

Cells were collected using the RNeasy Mini Kit (Qiagen - 74106) or the NucleoSpin 8 RNA Core Kit (Macherey-Nagel - 740465.4) for total RNA extraction, according to manufacturer’s instructions, and contaminant DNA was removed with rDNase Set (Macherey-Nagel, 740963) or RNase-Free DNase Set (Qiagen – 79254).

Complementary DNA (cDNA) was prepared using oligo(dT)-primed MoMLV Reverse Transcriptase (Invitrogen, 28025-013), following the manufacturer’s instructions. Gene expression levels were quantified by FastStart SYBR Green Master Mix (Roche) on a QuantStudio 5 (Applied Biosystems, Thermo Fisher Scientific) real-Time PCR Detection System and analysed with QuantStudio Design and Analysis software (version 1.4.3).

Expression levels were calculated relative to *RPLP0*, unless otherwise specified. Human and murine RT-qPCR primer sequences are listed in Supplementary Table 7.

Chromatin immunoprecipitation-qPCR

ChIP was performed as previously described[27]. Briefly, cells were crosslinked with 1% formaldehyde (Sigma) in culture medium for 10 minutes at RT, and chromatin from lysed nuclei was sheared to 200–600 bp fragments using a Branson Sonifier 450 A. For ChIP-qPCR, ~100 µg of sheared chromatin and 3-5µg of antibody were used. Antibody/antigen complexes were recovered with ProteinA-Dynabeads (ThermoFisher) for 2 hours at 4 °C. Where indicated, cells were transfected with siRNA for YAP and TAZ and processed for ChIP 48 hours later. Quantitative real-time PCR was carried out with QuantStudio 5 thermal cycler (ThermoFisher); each sample was analyzed in triplicate. The amount of immunoprecipitated DNA in each sample was determined as the fraction of the input (amplification efficiency$^{(\text{Ct INPUT} - \text{Ct ChIP})}$), and normalized to the immunoglobulin G control. The list of antibodies used for ChIP-qPCR and the corresponding dilutions are provided in Supplementary Table 4. Human Chip-qPCR primer sequences are listed in Supplementary Table 7.

The ChIP-Seq profiles for YAP in human NCI-H2052 and human IMR-90 fibroblasts[77] were retrieved from GSE61852 and visualized using Integrative Genomic Viewer (freeware from the Broad Institute) version 2.6.1.

SA-β-Gal Staining

Senescence-associated β-Galactosidase (SA-β-Gal) activity was detected using Senescence β-Galactosidase Staining Kit (Cell Signaling TECHNOLOGY – 9860), according to the manufacturer's instructions.

Soft and Stiff hydrogels

For the preparation of soft (0.5 kPa) and stiff (40 kPa) polyacrylamide hydrogels, two different solutions of Acrylamide (AA, Sigma-Aldrich), N,N′-Methylenebis(acrylamide) (BAA, Sigma-Aldrich) and N-Hydroxyethyl acrylamide (AA-OH, Sigma-Aldrich) were prepared in milliQ water. The reagents were mixed to final w/v % concentrations of AA, AA-OH and BAA of: 2.75, 1.21 and 0.03 for soft hydrogels and 7.25, 1.21 and 0.48 for stiff hydrogels. Polymerization was initiated adding 1:1000 (v/v) of (N,N,N′,N′-Tetramethylethylenediamine (TEMED, Sigma-Aldrich) and 0.1% (w/v) or 0.2% (w/v) of Ammonium persulfate (APS, Sigma-Aldrich) for stiff and soft gels respectively. Before gelification, the solution was pipetted in Polydimethylsiloxane rings, placed on a Kapton film, which were then covered with glass coverslips, previously silanized with 3-(Trimethoxysilyl)propyl methacrylate (TMSPM, Sigma Aldrich). Swelling and functionalization of the hydrogels were carried out by overnight incubation with a 25 μg/mL fibronectin solution in PBS. Soft and stiff gels were then washed twice in PBS and cells were seeded in a drop of complete culture medium and harvested and processed after 36 hours.

Micropatterns

Micropatterned glass substrates were prepared by UV photolithography. A positive photoresist (S1805 G2, Microchem) was spin coated on glass coverslips, previously silanized with 3- (Trimethoxysilyl)propyl methacrylate (TMSPM, Sigma Aldrich). The film was then patterned by UV exposure (collimated lamp at 365nm) through a bright-field chrome photomask and developed with MF-319 (Microchem), achieving squares of photoresist. Linear polyacrylamide was then grafted on the patterned surface of the glass, polymerizing an 8% w/v solution of acrylamide in milliQ water with 0.0225% w/v of APS and 15:1000 v/v of TEMED. The substrates were left overnight in water to wash out unreacted reagents. Finally, the resist was stripped by dipping the substrates in acetone, DMSO and milliQ water; the coverslips were UV sterilized, and the adhesive islands were functionalized incubating a 10 μg/mL fibronectin solution for 1 hour at 37 °C. Micropatterned coverslips were washed twice in PBS and cells were seeded in complete culture medium.

Statistics and reproducibility

Data are shown as indicated in figure legends. Statistical tests (two-sided, unpaired *t*-test and one way-ANOVA with Dunnett's multiple comparison test) are indicated in figure legends and were performed with GraphPad Prism8.4.3 software, and only on biological replicates. Sample sizes are stated in the corresponding figure legends. No statistical method was used to predetermine sample size.

All tested animals were included in the analysis. All experiments were reproducible. Mice were randomly allocated to experimental or treatment groups. Investigators were not blinded to mouse grouping because animal experiments and assessment of their health status were performed by the same researchers. Instead, pathological examination of histological section was carried out by M. Fassan (a professional pathologist) who was blind to animal treatments.

For experiments not involving mice, the investigators were not blinded because analyses relied on unbiased measurements of quantitative parameters. However, standardized procedures for data collection and analysis were used to prevent bias.

The experiments shown in Fig. 2a and Extended Data Fig. 3a, b were repeated four times independently with similar results. The experiments shown in Extended Data Fig. 2a, g, Extended Data Fig. 5h were repeated two times independently with similar results. The experiments shown in Extended Data Fig. 8a were repeated five times independently with similar results.

Extended Data

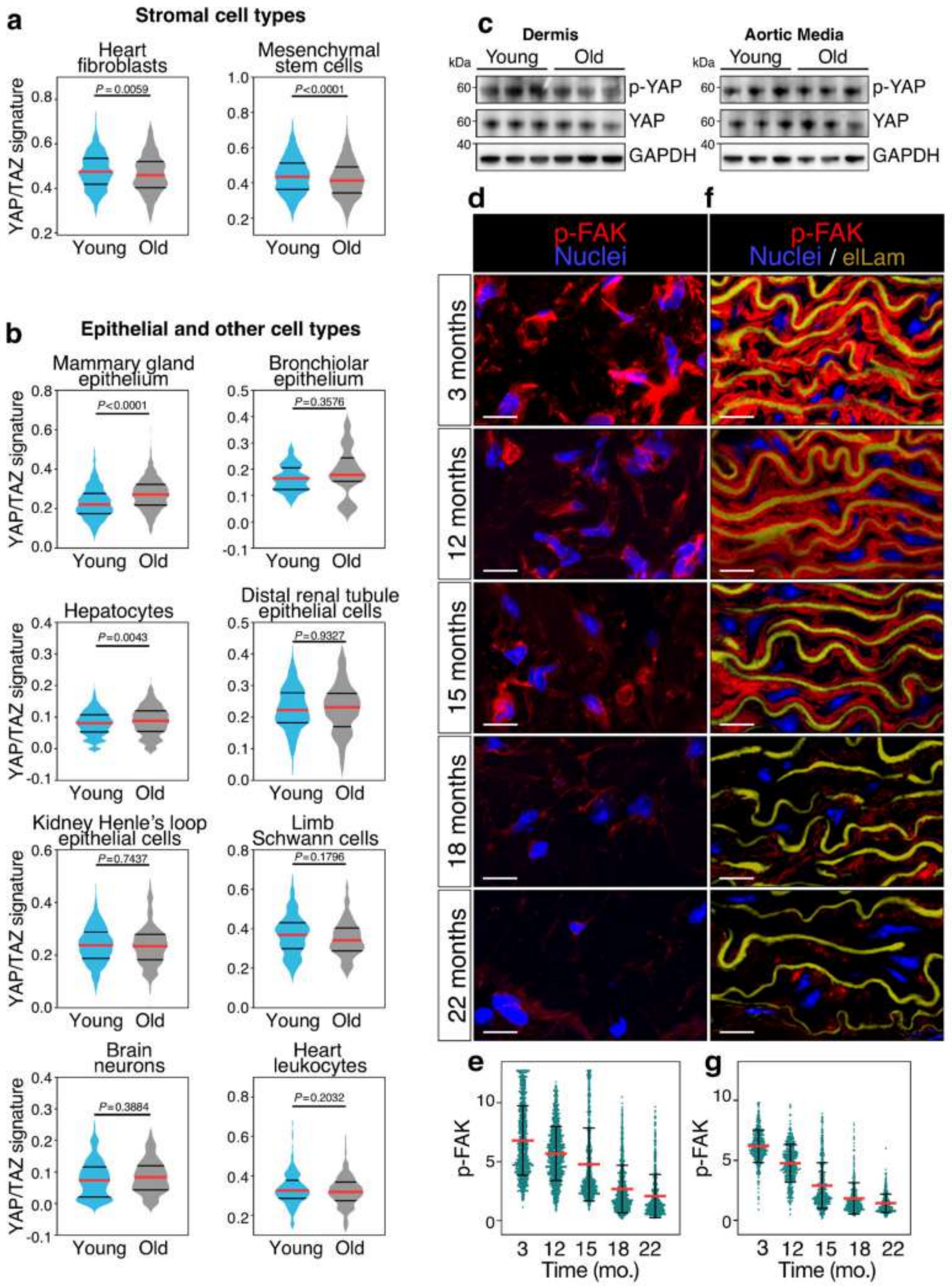

Extended Data Fig. 1. Natural aging correlates with loss of YAP/TAZ mechanotransduction in connective tissues.

a, **b**, Violin plots showing the distribution of the YAP/TAZ activity signature expression in the indicated cell types form young and old mice. Heart fibroblasts (young n= 476 cells; old n= 511 cells), mesenchymal stem cells (young n= 3824 cells; old n= 4249 cells), mammary gland epithelial cells (young n= 873 cells; old n= 1196 cells), bronchiolar epithelial cells (young n= 44 cells; old n= 15 cells), hepatocytes (young n= 2304 cells; old n= 358 cells), distal renal tubule epithelial cells (young n= 225 cells; old n= 147 cells), Henle's loop epithelial cells (young n= 870 cells; old= 346 cells), Schwann cells (young n= 109 cells; old n= 93 cells), brain neurons (young n= 83 cells; old n= 59 cells), and heart leukocytes (young n= 139 cells; old n= 187 cells) were retrieved from *Tabula Muris Senis* (as in Fig.1b). Red lines denote the median, black lines denote quartiles. *P* values are derived from two-sided, unpaired t-test with Welch's correction.

c, Immunoblotting analysis of YAP and phospho-YAP (p-YAP) in dermal (left panel) and aortic (right panel) samples from young and old mice (n=3 mice per age and tissue). GAPDH served as loading control.

d, **f**, Representative immunofluorescence staining for phospho-FAK (p-FAK) in dermal fibroblasts (**d**) and aortic wall (**f**) of wild-type mice of the indicated ages. elLam is elastic lamellae. Bar=10 µm.

e, **g**, Quantification of the p-FAK signal in dermal fibroblasts (**e**, related to **d**) and aortic smooth muscle cells (**g**, related to **f**) of wild-type mice of the indicated ages. Data are shown as mean (red line) ± s.d. At least 400 cells per condition were analyzed from 3 independent mice. *P* values are derived from one-way ANOVA with Dunnett's multiple comparison test. $P<0.0001$ in all conditions compared to 3-month-old mice.

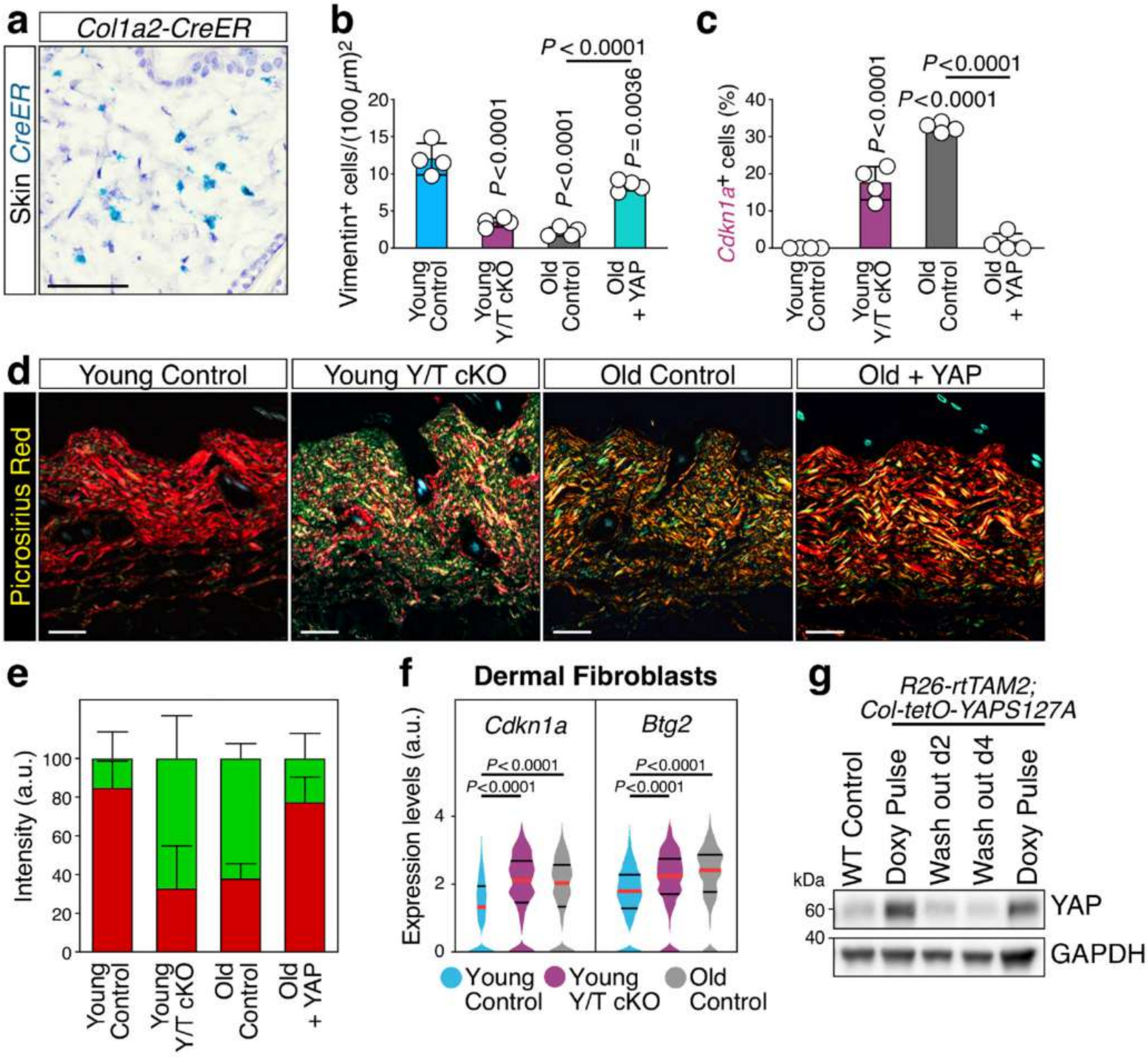

Extended Data Fig. 2. YAP/TAZ in dermal fibroblasts control dermal and ECM homeostasis.

a, Representative *in situ* hybridization for Cre recombinase (*CreER*) in dorsal skin sections of a *Col1a2-CreER* mouse, showing specific staining in dermal fibroblasts (bar=50 μm).

b, Quantification of Vimentin-positive cells in the dermal layer of skin sections from mice of the indicated genotypes. Data (n=4 mice for each column) are presented as mean ± s.d.; *P* values are derived from one-way ANOVA with Dunnett's multiple comparison test. Related to Fig. 2b.

c, Quantification of *Cdkn1a*-positive cells in the dermal layer of skin sections from mice of the indicated genotypes. Data (n=4 per condition) are presented as mean ± s.d.; *P* values are derived from one-way ANOVA with Dunnett's multiple comparison test. Related to Fig. 2c.

d, **e**, Representative birefringence images (**d**, bar=100 μm) and quantification (**e**) of picrosirius red staining on dorsal skin sections from mice of the indicated genotypes. In **d**, the red-to-green gradient reflects the decreasing thickness of collagen fiber bundles. In **e**, red is the quantification of thicker collagen fibers appearing as red or yellow in birefringence; green is the quantification of thinner fibers appearing as green in the same conditions. Data in **e** (n=4 mice for each column) are presented as mean + s.d., 25 areas were analyzed per condition.

f, Violin plots from sc-RNA seq data showing the expression distribution of *Cdkn1a* and *Btg2* in freshly dissociated dermal fibroblasts of young control (n=2916 cells), young Y/T cKO (n=759 cells) and old control (n=1413 cells) mice. Red lines denote the median, black lines denote quartiles. *P* values are derived from Kruskal-Wallis test.

g, Immunoblotting analysis of YAP in tail tip biopsies from wild-type (WT Control) and *R26-rtTAM2; Col-tetO-YAPS127A* mice treated with intermittent doxycycline regime to sustain YAP activity. Mice were analyzed under doxycycline (Doxy Pulse) or during the off-doxy period, two or four days after the last doxy pulse (Wash out d2 and Wash out d4, respectively; see Methods). GAPDH served as loading control.

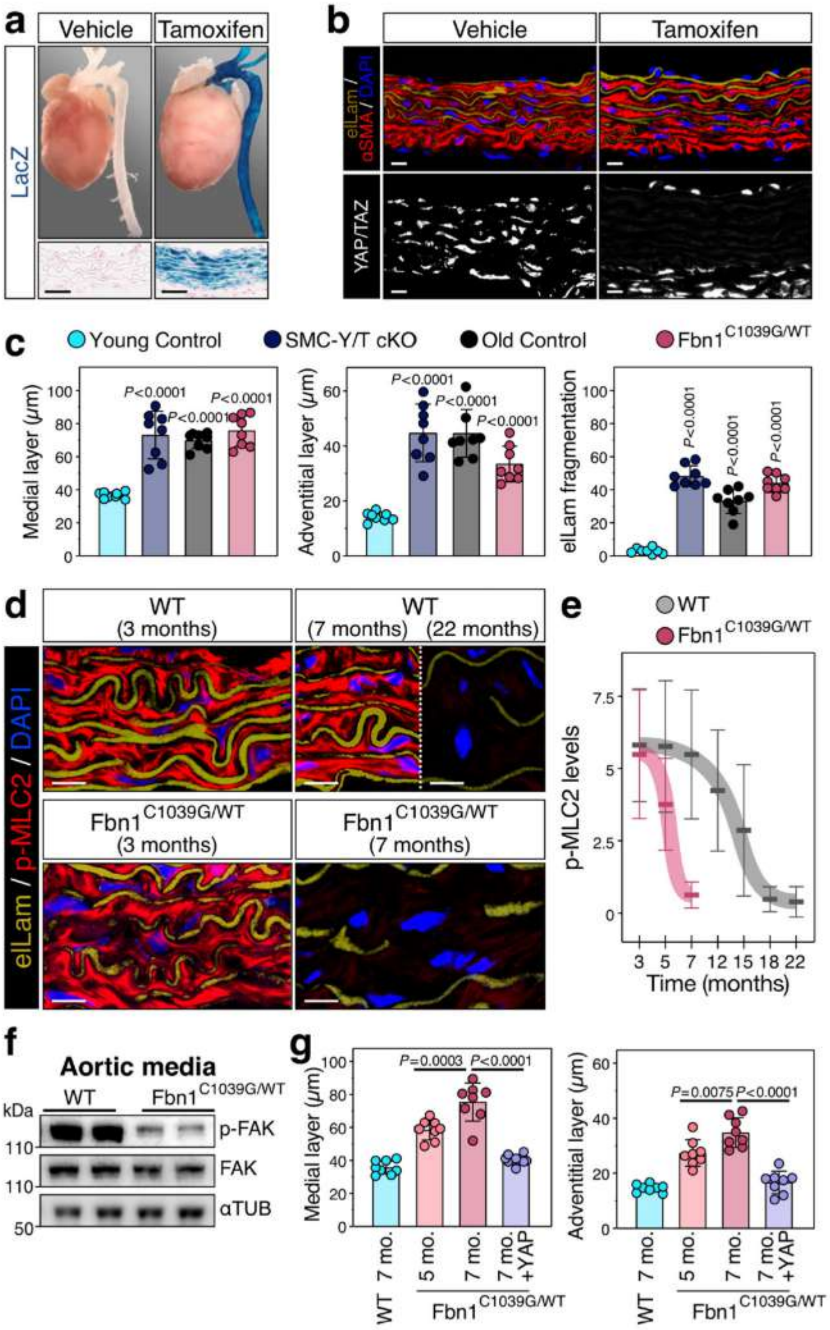

Extended Data Fig. 3. Additional characterization of the role of YAP/TAZ mechanotransduction in preserving aortic wall integrity.

a, Whole mount X-Gal staining in heart and aorta (upper panel) and aortic wall sections (lower panel, bar=50 μm) of *SmmhcCreER; R26-LSL-LacZ* mice, either treated with Tamoxifen or Vehicle. Blue signal confirms the inducible and highly specific activity of the Cre driver in vascular smooth muscle cells.

b, Representative immunofluorescence staining for alpha-smooth muscle actin (αSMA, upper panel) and YAP/TAZ (lower panel) in the aortic wall of *SmmhcCreER; YAP*$^{fl/fl}$*;*

TAZ$^{fl/fl}$ mice, showing YAP/TAZ ablation in vascular smooth muscle cells exclusively after Tamoxifen treatment. Bar=10 μm.

c, Quantification of medial layer thickness, adventitial layer thickness and elLam fragmentation of mice of the indicated genotypes. Young control are 7-month-old wild-type mice, Old Control are >21-month-old wild-type mice. Related to Fig. 3a. Data (n=8 mice for each column) are presented as mean ± s.d.; *P* values are derived from one-way ANOVA with Dunnett's multiple comparison test.

d, **e**, Representative immunofluorescence staining for p-MLC2 (**d**, bar=10 μm) and quantification (**e**) of p-MLC2 levels in the aortic wall of wild-type (WT) and *Fbn1*$^{C1039G/WT}$ mice of the indicated ages. elLam is elastic lamellae. Quantification data are presented as mean ± s.d. *P* values are derived from one-way ANOVA with Dunnett's multiple comparison test. $P<0.0001$ in all conditions compared to 3-month-old wild-type mice, except for 3-month-old *Fbn1*$^{C1039G/WT}$ mice ($P=0.0092$). The number of cells analyzed for each mouse strain and age is reported in the corresponding source data file (where n is >400 for each point).

f, Immunoblotting analysis of total FAK and phospho-FAK (p-FAK) in adventitia-denuded aortic samples from wild-type and 7-month-old *Fbn1*$^{C1039G/WT}$ mice. α-Tubulin (αTUB) served as loading control. Two mice per condition are shown.

g, Quantification of medial layer thickness and adventitial layer thickness in aortic sections of wild-type, *Fbn1*$^{C1039G/WT}$ and *Fbn1*$^{C1039G/WT}$ + YAP mice, as in Fig. 3f. Data (n=8 mice for each group) are presented as mean ± s.d.; *P* values are derived from one-way ANOVA with Dunnett's multiple comparison test.

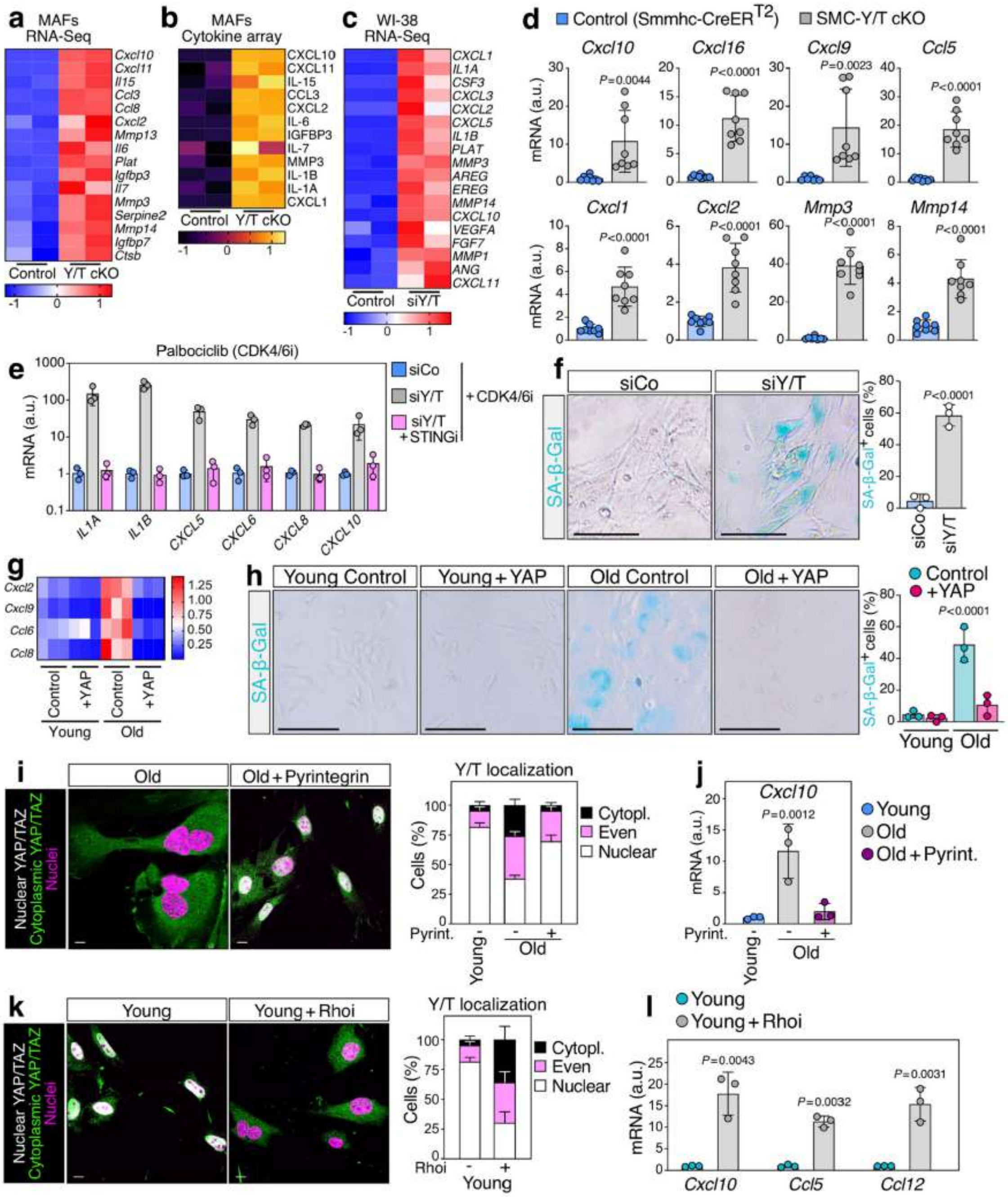

Extended Data Fig. 4. YAP/TAZ oppose senescence in stromal cells.

a, **b**, Heatmaps showing transcriptional induction (**a**) and secretion (**b**) of SASP factors after ex vivo genetic ablation of YAP/TAZ (Y/T cKO) in primary mouse adult fibroblasts (MAFs). Secretion of TNFα, a necrosis marker, was not detected.

c, Heatmaps showing upregulation of SASP in WI-38 human fibroblasts upon siRNA-mediated depletion of YAP/TAZ (siY/T). *TNFA* expression was not detected.

d, RT-qPCR analysis showing induction of SASP marker genes in adventitia-denuded aortic media from SMC-Y/T cKO compared to control mice. Data (n=8 mice per column) are presented as mean ± s.d.; *P* values are derived from two-sided, unpaired t-test.

e, RT-qPCR analysis of SASP marker genes in control (siCo) and YAP/TAZ-depleted (siY/T) WI-38 cells, treated with CDK4 inhibitor (CDK4i, 4 μM Palbociclib for 48 hours), with or without concomitant STING inhibition (STINGi, 1 μM H-151 for 48 hours). Data (n=3 independent experiments) are shown as mean ± s.d.

f, Senescence-associated β-galactosidase (SA-β-Gal) staining (left panel, bar=50 μm) and quantification (right panel, n=3 independent experiments) in WI-38 cells upon depletion of YAP/TAZ (siY/T). Quantification data are presented as mean ± s.d.; *P* values are derived from two-sided, unpaired t-test.

g, Heatmap showing upregulation of SASP marker genes in primary old MAFs, rescue by YAP-add back, as assessed by RT-qPCR. MAFs were isolated from young and old *R26-rtTAM2; Col-tetO-YAPS127A* mice, left untreated (Control) or treated with doxycycline (+ YAP) to sustain YAP activity ex vivo. Related to Fig. 4b.

h, SA-β-Gal staining (left panel, bar=50 μm) and quantification (right panel, n=3 independent experiments) in primary MAFs isolated from young (3 months) and old (>21 months) mice, in the presence or absence of constitutively active YAP5SA (+ YAP). Cells transduced with empty vector are indicated as Control. Quantification data are presented as mean ± s.d.; *P* values are derived from one-way ANOVA with Dunnett's multiple comparison test.

i, Immunofluorescence staining for YAP/TAZ (Y/T) (left panel, bar=10 μm) and quantification of subcellular Y/T distribution (right panel, n=3 independent experiments) in freshly isolated MAFs from old (>21 months) mice, either control or treated with Pyrintegrin (3.5 μM for 24 hours). Data are displayed as mean ± s.d.

j, RT-qPCR analysis of *Cxcl10* in primary MAFs isolated from young (3 months) and old (>21 months) mice, the latter either control or treated with Pyrintegrin (3.5 μM for 24 hours). Data (n=3 independent experiments) are presented as mean ± s.d.; *P* values are derived from one-way ANOVA with Dunnett's multiple comparison test.

k, Immunofluorescence staining for YAP/TAZ (Y/T) (left panel, bar=10 μm) and quantification of subcellular Y/T distribution (right panel, n=3 independent experiments) in freshly isolated MAFs from young mice, either control or treated with Rho inhibitor (Rhoi, 0.5 μg/ml C3 for 24 hours). Quantification data are displayed as mean ± s.d.

l, Expression of SASP markers in young MAFs either control or treated with Rhoi, as assessed by RT-qPCR. Data (n=3 independent experiments) are shown as mean ± s.d.; *P* values are derived from two-sided, unpaired t-test.

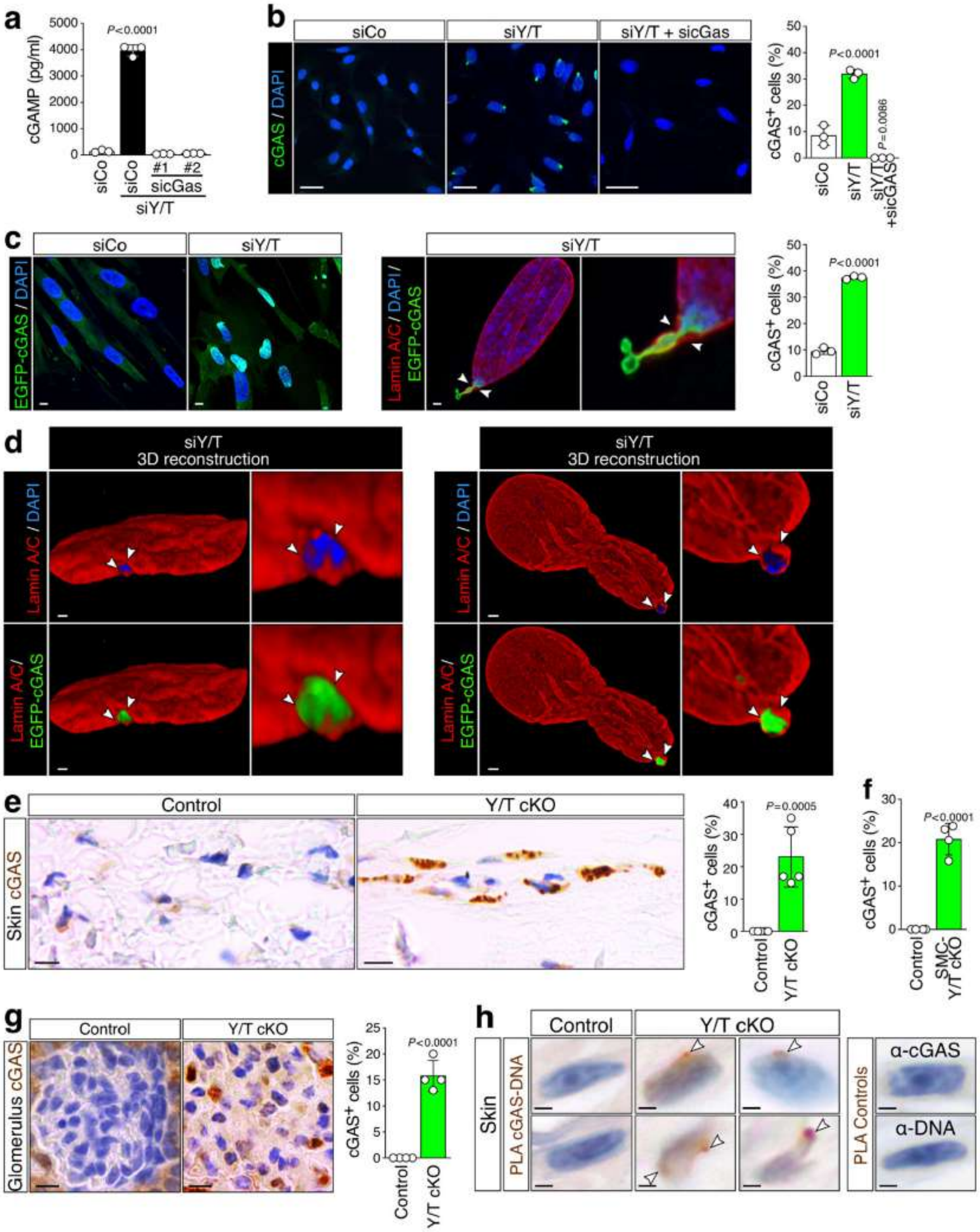

Extended Data Fig. 5. YAP/TAZ loss triggers cGAS activation on genomic DNA.

a, cGAMP levels in control (siCo) or YAP/TAZ-depleted (siY/T) primary mouse aortic smooth muscle cells, as assessed by ELISA. Concomitant cGAS depletion (sicGAS #1 and #2) served as specificity control. Data (n=3 independent experiments) are shown as mean ± s.d.; P values are derived from one-way ANOVA with Dunnett's multiple comparison test. **b,** Immunofluorescence staining (left panel, bar=20 μm) and quantification (right panel, n=3 independent experiments) for endogenous cGAS in freshly isolated control (siCo) and YAP/TAZ-depleted (siY/T) MAFs. Concomitant cGAS depletion (siY/T + sicGas) served as specificity control. Data are presented as mean ± s.d.; *P* values are derived from one-way ANOVA with Dunnett's multiple comparison test.

c, Confocal images (left panel, bar=10 µm), superresolution microscopy analysis (middle panel, bar= 1 µm. Arrowheads indicate sites of genomic DNA herniation through the nuclear Lamina (Lamin A/C)) and quantification (right panel, n=3 independent experiments) of EGFP-cGAS reporter signal in control (siCo) and YAP/TAZ-depleted (siY/T) WI-38 cells. Quantification data are shown as mean ± s.d; *P* values are derived from two-sided, unpaired t-test.

d, 3D reconstruction of immunofluorescence-labeled (Lamin A/C) nuclei of YAP/TAZ-depleted (siY/T) WI-38 cells, expressing the EGFP-cGAS reporter. Arrowheads indicate EGFP-cGAS recruitment at site of genomic DNA (DAPI) herniations. Bar=1 µm.

e, Low magnification/field view of endogenous cGAS IHC staining in the dermis of control and Y/T cKO mice (left panel, bar=10 µm). Quantifications (right panel, n=5 mice) are shown as mean ± s.d.; *P* values are derived from two-sided, unpaired t-test.

f, Quantification of cGAS-positive aortic smooth muscle cells from control and SMC-Y/T cKO mice. Data (n=4 mice per column) are shown as mean ± s.d.; *P* values are derived from two-sided, unpaired t-test. Related to Fig. 4g.

g, IHC staining (left panel, bar=10 µm) and quantification (right panel, n=4 mice per column) of endogenous cGAS protein in kidney glomerulus of control and Y/T cKO mice. Quantification data are shown as mean ± s.d; *P* values are derived from two-sided, unpaired t-test.

h, In vivo PLA detection (arrowheads, left panel, bar=1 µm) of physical association of endogenous cGAS with nuclear DNA in dermal fibroblasts of control and YAP/TAZ cKO mice (respectively, 2% and 19% of PLA-positive cells, n>30 cells). Single antibodies (α-cGAS and α-DNA) run in the same assay gave no signal whatsoever, and representative pictures of these negative controls are shown in the right panel.

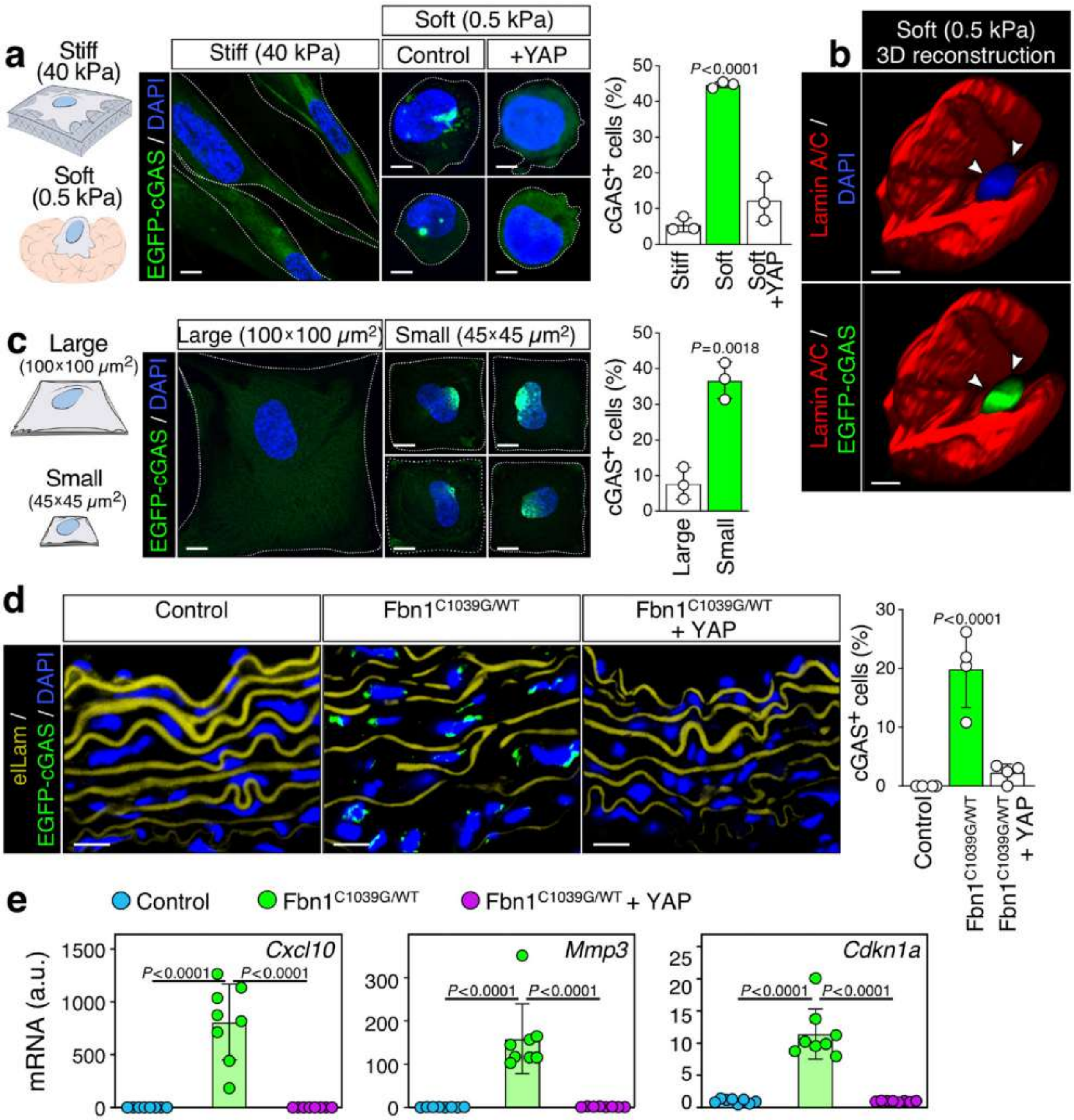

Extended Data Fig. 6. YAP/TAZ mechanotransduction suppresses cGAS activation.

a, EGFP-cGAS reporter signal (left panel, bar=10 μm) and quantification (right panel, n=3 per condition) in WI-38 cells seeded on stiff (40 kPa) and soft (0.5 kPa) hydrogels in presence or absence of experimentally sustained YAP activity (+YAP). Cell boundaries are indicated by dotted lines. Quantification data are presented as mean ± s.d.; *P* values are derived from one-way ANOVA with Dunnett's multiple comparison test.

b, 3D reconstruction of a representative nucleus from WI-38 cells expressing the EGFP-cGAS reporter seeded on soft (0.5 kPa) hydrogels and then stained with Lamin A/C and DAPI. Arrowheads indicate EGFP-cGAS accrual at site of genomic DNA (DAPI) herniation. Bar=2 µm.

c, EGFP-cGAS reporter signal (left panel, bar=10 µm) and quantification (right panel, n=3 independent experiments) in WI-38 cells plated on large and small adhesive microislands. Cell boundaries are indicated by dotted lines. Quantification data are presented as mean ± s.d.; *P* values are derived from two-sided, unpaired *t*-test.

d, Representative immunofluorescence staining (left panel, bar=10 µm) and quantification (right panel, n=4 mice) of endogenous cGAS in the aortic wall of mice of the indicated experimental groups. elLam is elastic lamellae. Note perinuclear activation of endogenous cGAS in the aortic mediae of $Fbn1^{C1039G/WT}$ mice, and its prevention by sustaining YAP activity ($Fbn1^{C1039G/WT}$+YAP) in aortic smooth muscle cells. Data are presented as mean ± s.d.; *P* values are derived from one-way ANOVA with Dunnett’s multiple comparison test.

e, RT-qPCR analysis of senescence markers in adventitia-denuded aortic mediae from mice of the indicated genotypes. Data (n=8 mice per column) are presented as mean ± s.d.; *P* values are derived from one-way ANOVA with Dunnett’s multiple comparison test.

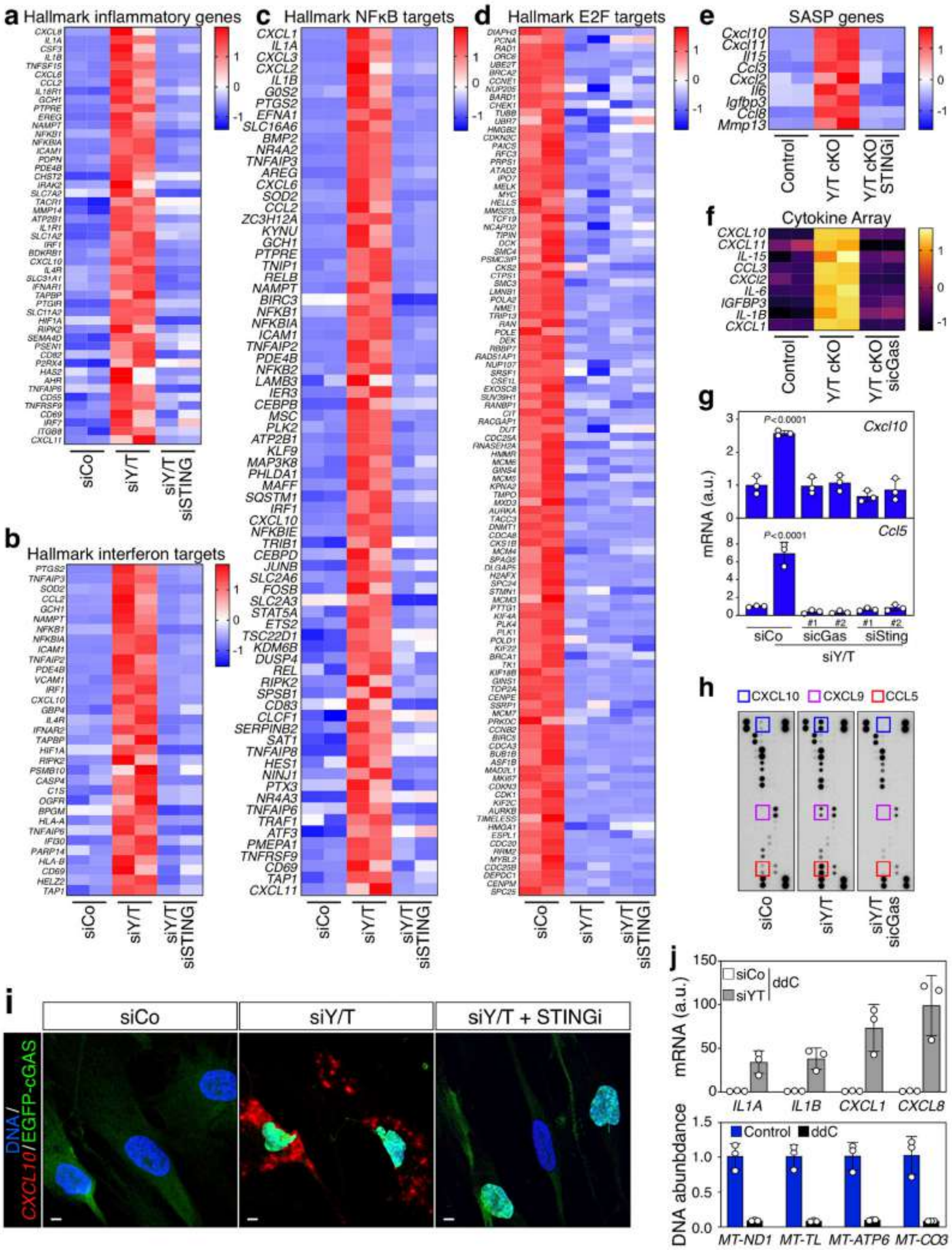

Extended Data Fig. 7. YAP/TAZ loss induces SASP induction through cGAS/STING signalling.

a-c, Heatmap showing the STING-dependent induction of inflammatory genes (**a**), interferon target genes (**b**) and NF-kB target genes (**c**) upon YAP/TAZ depletion in WI-38 fibroblasts, as determined by RNA-seq.

d, Heatmap showing that E2F target genes are downregulated upon YAP/TAZ depletion in WI-38 cells independently of STING, as determined by RNA-seq.

e, Heatmap portraying the STING-signalling dependency of SASP marker induction upon genetic ablation of YAP/TAZ (Y/T cKO) in primary MAFs. STINGi is H-151 (1 μM).

f, Heatmap displaying cGAS-dependent cytokine secretion upon genetic ablation of YAP/TAZ in primary MAFs.

g, RT-qPCR for SASP marker genes upon YAP/TAZ depletion (siY/T) in mouse aortic smooth muscle cells, with or without concomitant cGAS (sicGas#1 and #2) or STING (siSting#1 and #2) depletion. Data (n=3 independent experiments) are presented as mean ± s.d.; *P* values are derived from one-way ANOVA with Dunnett's multiple comparison test.

h, Cytokine array showing cGAS-dependent secretion of the indicated SASP cytokines upon YAP/TAZ ablation in primary mouse aortic smooth muscle cells. Spots in the upper left and right corners and in the lower right corner served as reference.

i, *In situ* hybridization for *CXCL10* in control (siCo) and YAP/TAZ-depleted (siY/T) WI-38 cells, expressing EGFP-cGAS reporter. Treatment with STING inhibitor (STINGi, 1 μM H-151 for 48 hours) served as negative control. Bar=2 μm. Percentage of cells showing concomitant EGFP-cGAS activation and *CXCL10* mRNA expression were 0% in siCo, 35% in siY/T and 0% in siY/T + STINGi conditions. At least 40 cells were analyzed for each condition.

j, Upper panel, RT-qPCR for SASP marker genes in YAP/TAZ-depleted (siY/T) and control (siCo) WI-38 cells, treated with 2',3'-dideoxycytidine (ddC, 5 μM for 1 week). Lower panel, qPCR for mitochondrial genes confirming mtDNA depletion by ddC treatment. Note that mtDNA is not required for SASP induction after Y/T depletion. Data (n=3 independent experiments) are presented as mean ± s.d.

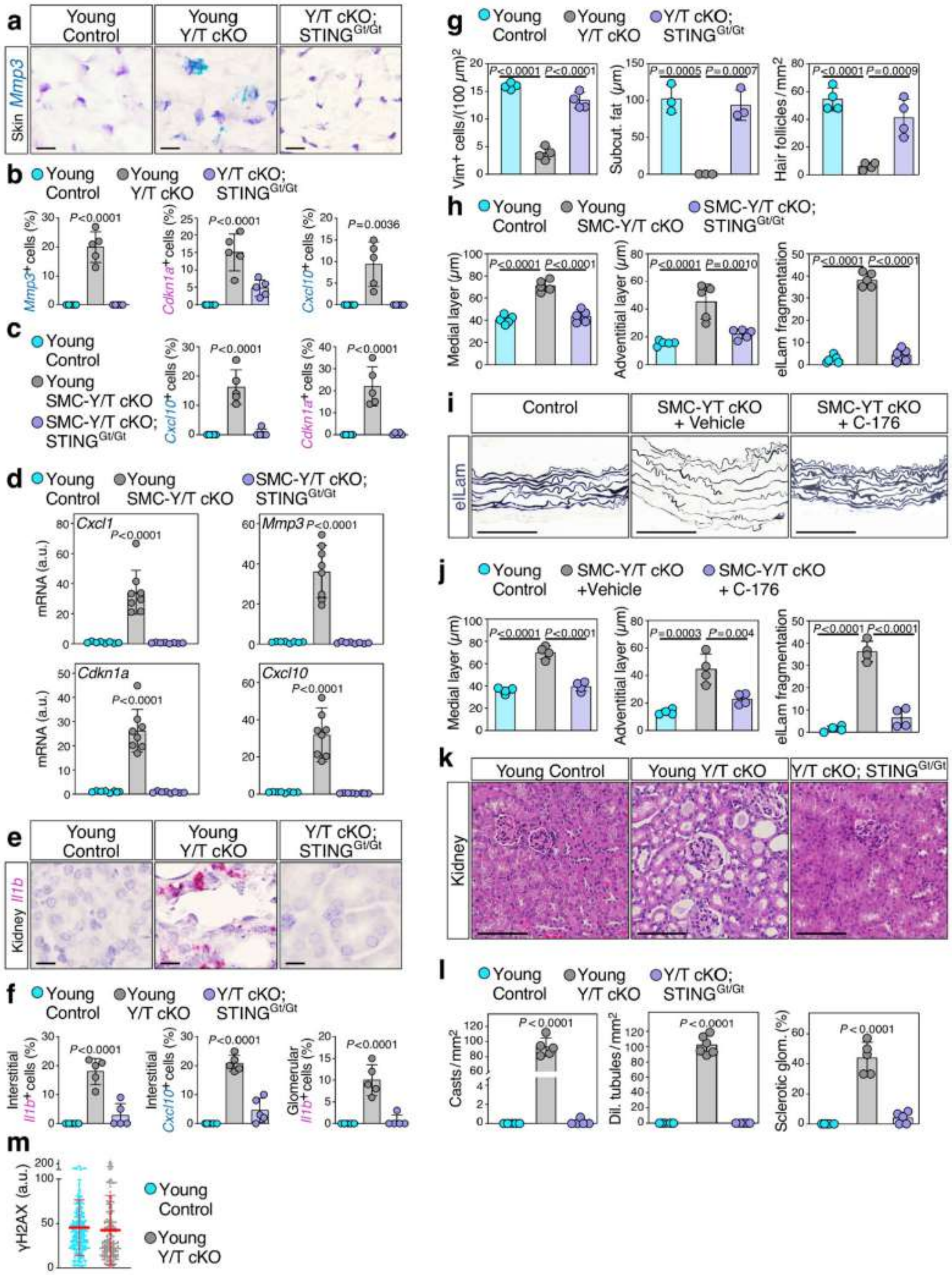

Extended Data Fig. 8. cGAS-STING signalling drives senescence-traits and age-related pathology downstream of YAP/TAZ inactivation in connective tissues.

a, Representative ISH for *Mmp3* (bar=10 μm) in the dermis from mice of the indicated genotypes. **b**, **c**, Quantification (n=5 mice per column) of the ISH signal for the indicated SASP markers in the dermis (**b,** related to **a**, and to Fig. 4i) and aorta (**c,** related to Fig. 4j) from mice of the indicated genotypes. Data are presented as mean ± s.d.; *P* values are derived from two-sided, unpaired t-test. **d**, RT-qPCR analysis showing induction of SASP marker genes in aortic mediae of SMC-Y/T cKO mice, prevented by STING loss-of-function mutation (SMC-Y/T cKO; STING$^{Gt/Gt}$). Data (n=8 mice per column) are presented as mean ± s.d.; *P* values are derived from one-way ANOVA with Dunnett’s multiple comparison test.

e, **f**, Representative ISH for *Il1b* (**e,** bar=10 μm) and quantification (**f**, n=5 mice) of the ISH signal for the indicated SASP markers in kidney sections from young control, Y/T cKO and Y/T cKO; STING$^{Gt/Gt}$ mice. Quantification data are presented as mean ± s.d.; *P* values are derived from one-way ANOVA with Dunnett’s multiple comparison test. Related to Fig. 4k.

g, Quantification of Vimentin-positive cells (n=4 mice per column), subcutaneous fat layer thickness (n=3 mice) and hair follicle density (n=4 mice) in skin sections of mice of the indicated genotypes. Related to Fig. 4l. Data are presented as mean ± s.d.; *P* values are derived from one-way ANOVA with Dunnett’s multiple comparison test.

h, Quantification of medial layer thickness, adventitial layer thickness and elastic lamellae fragmentation of aortic sections from mice of the indicated genotypes. Related to Fig. 4m. Data (n=5 mice per column) are presented as mean ± s.d.; *P* values are derived from one-way ANOVA with Dunnett’s multiple comparison test.

i, **j**, Representative elLam staining (**i**, bar=100 μm) and quantification (**j**, n=4 mice per column) of medial layer thickness, adventitial layer thickness and elLam fragmentation in aortic sections from control mice, and SMC-Y/T cKO mice either treated with Vehicle or with the STING inhibitor C-176. Data are presented as mean ± s.d.; *P* values are derived from one-way ANOVA with Dunnett’s multiple comparison test.

k, **l**, Representative images of H&E-stained (**k**, bar=100 μm) kidney sections of mice of the indicated genotype. Quantification (**l**) of intratubular casts (n=5 mice per column), dilated tubules (n=6 mice per column) and sclerotic glomeruli (n=5 for mice per column) are presented as mean ± s.d.; *P* values are derived from one-way ANOVA with Dunnett’s multiple comparison test.

m, Quantification of γH2AX signal in dermal fibroblasts of control and YAP/TAZ cKO mice. The number of cells analyzed for each condition is reported in the corresponding source data file (n>150 cells). Data are shown as mean ± s.d.; *P* values are derived from two-sided, unpaired *t*-test.

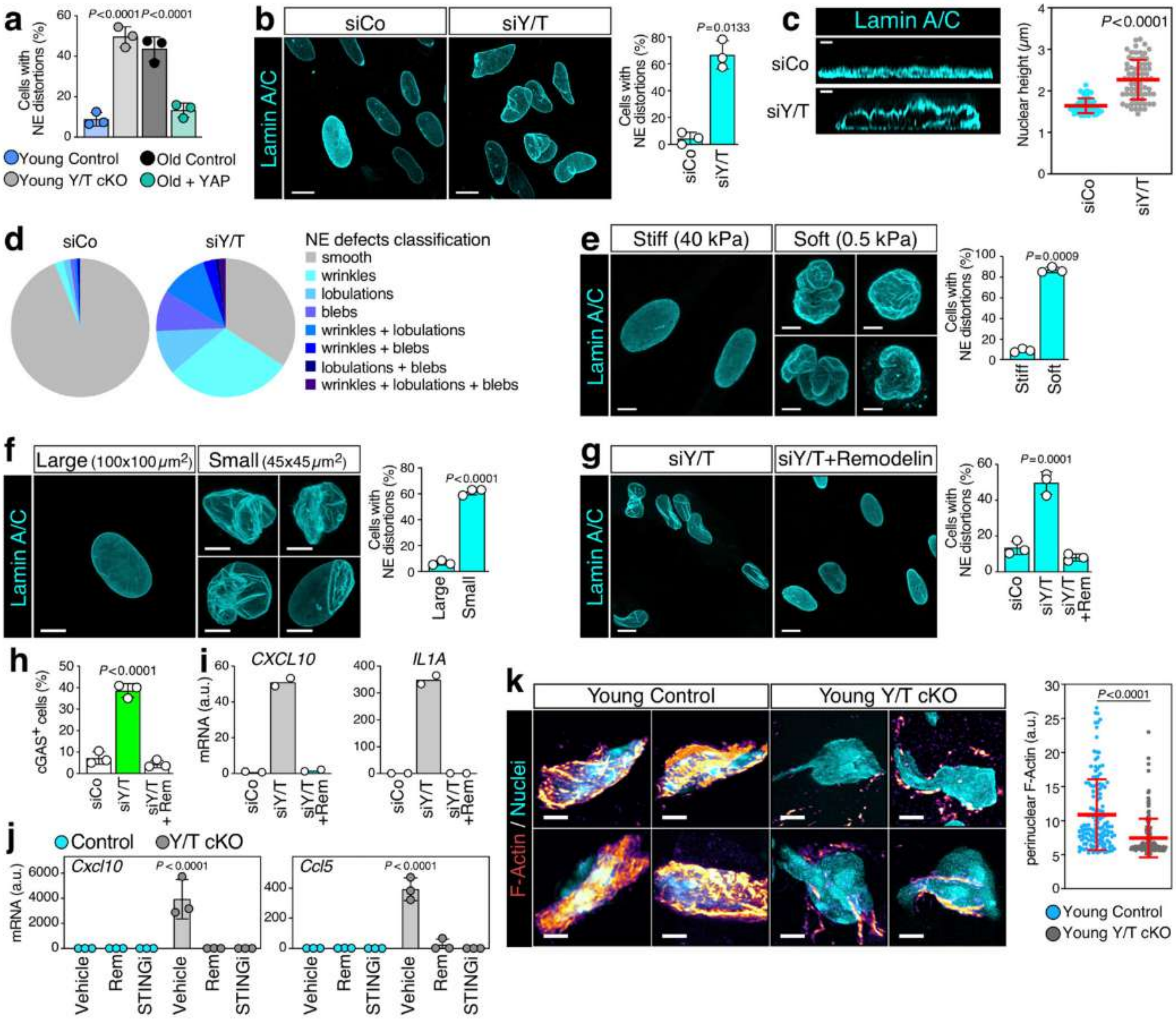

Extended Data Fig. 9. YAP/TAZ mechanotransduction is required to preserve NE architecture.

a, Quantification of nuclear dysmorphia (related to Fig.5a) in young control or YAP/TAZ-depleted MAFs, and in old MAFs with or without YAP reconstitution. Data (n=3 independent experiments) are presented as mean ± s.d.; *P* values are derived from one-way ANOVA with Dunnett's multiple comparison test.

b, Nuclear morphology (left panel) and quantification of nuclear dysmophia (right panel) in control (siCo) and YAP/TAZ-depleted (siY/T) WI-38 cells, as assessed by Lamin A/C immunostaining. Bar=10 μm. Data (n=3 independent experiments) are presented as mean ± s.d.; *P* values are derived from two-sided, unpaired *t*-test.

c, Orthogonal projection of Lamin A/C-stained nuclei (left panel, bar=1 μm) and quantification of nuclear height (right panel; n=70 cells per condition) in control or YAP/TAZ-depleted WI-38. Data are presented as mean ± s.d.; *P* values are derived from two-sided, unpaired *t*-test.

d, Pie charts showing the relative percentage of nuclear lamina defects upon Y/T depletion in WI-38 fibroblasts. At least 200 cells per condition were analyzed.

e, **f** Nuclear morphology (right panel) and quantification (left panels) of nuclear dysmorphia in WI-38 cells plated on stiff (40 kPa) or soft (0.5 kPa) hydrogels (**e**) and WI-38 cells plated on large or small microislands (**f**), as assessed by Lamin A/C immunostaining. Data (n=3 independent experiments) are presented as mean ± s.d.; *P* values are derived from two-sided, unpaired *t*-test. Bar=10 µm.

g, Nuclear morphology (left panel, bar=10 µm) and quantification (left panel) of nuclear dysmorphia in YAP/TAZ-depleted WI-38 cells, in presence or absence of Remodelin, as assessed by Lamin A/C immunostaining. Data (n=3 independent experiments) are shown as mean ± s.d.; *P* values are derived from one-way ANOVA with Dunnett's multiple comparison test.

h, Quantification of EGFP-cGAS reporter signal in YAP/TAZ-depleted (siY/T) WI-38 cells, with or without Remodelin treatment. Data (n=3 independent experiments) are shown as mean ± s.d.; *P* values are derived from one-way ANOVA with Dunnett's multiple comparison test. Related to Fig. 5b.

i, j SASP marker genes expression in WI-38 cells (**i**, n=2 independent experiments) and primary MAFs (**j**, n=3 independent experiments) upon YAP/TAZ depletion is abolished by concomitant Remodelin (Rem) treatment, as assessed by RT-qPCR analysis. In **j**, treatment with the STING inhibitor H-151 (STINGi) served as control. Data are shown as mean ± s.d.; *P* values are derived from one-way ANOVA with Dunnett's multiple comparison test.

k, In vivo super-resolution microscopy analysis (left panel, bar=1 µm) and quantification (right panel, at least n=130 cells per condition were analyzed) of perinuclear F-Actin in dermal fibroblasts of Control and YAP/TAZ cKO mice. Data are shown as mean ± s.d.; *P* values are derived from two-sided, unpaired *t*-test.

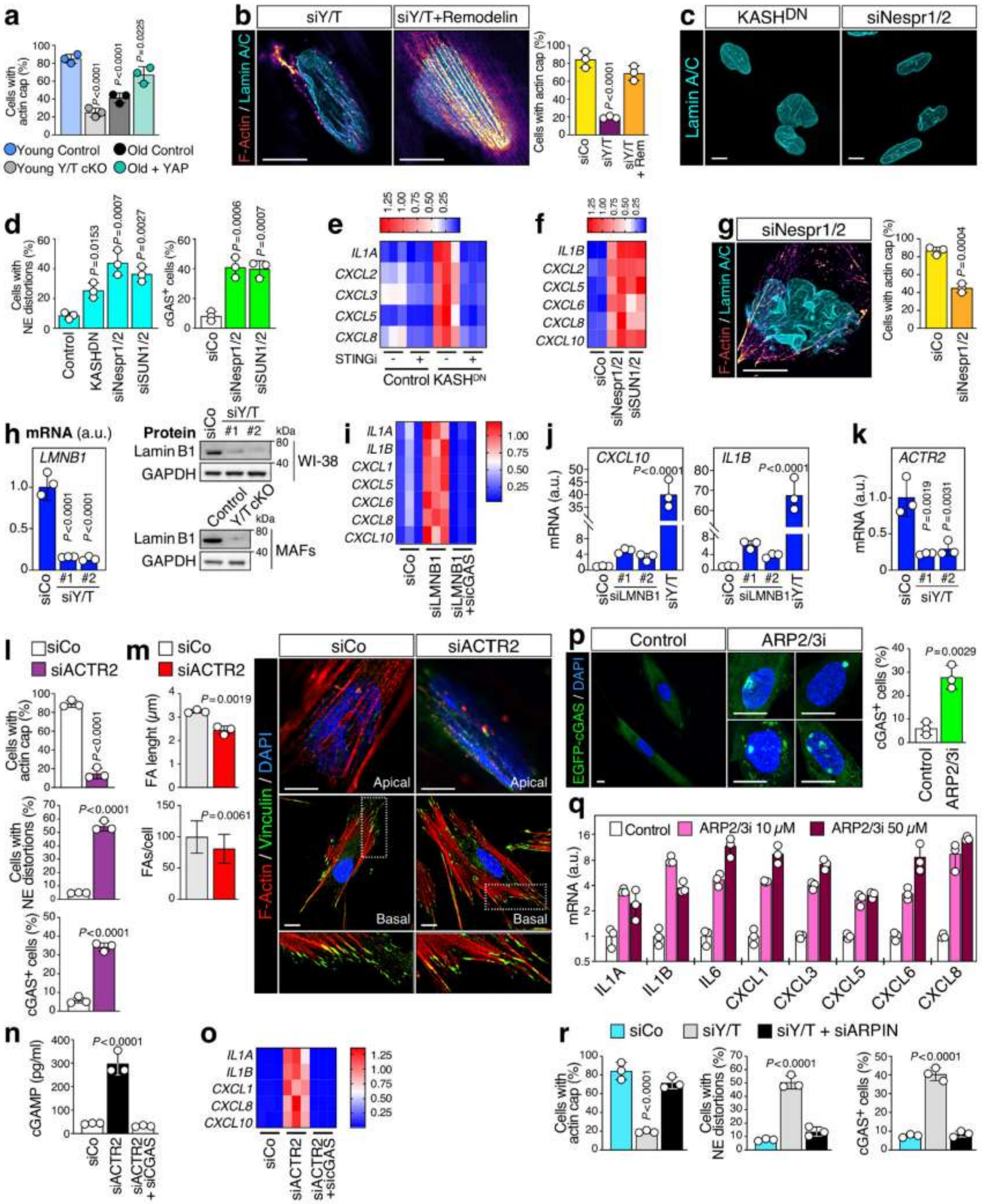

Extended Data Fig. 10. Role of the actin cap in preserving nuclear morphology downstream of YAP/TAZ.

a, Quantification of actin cap integrity (related to Fig. 5c) in young control or YAP/TAZ-depleted MAFs, and in old MAFs with or without YAP reconstitution. Data (n=3 independent experiments) are presented as mean ± s.d.; *P* values are derived from one-way ANOVA with Dunnett’s multiple comparison test.

b, Superresolution microscopy analysis (left panels) of actin cap integrity in YAP/TAZ-depleted WI-38 cells, in presence or absence of Remodelin, as assessed by F-Actin and

Lamin A/C staining. Apical sections are shown. Bar=10 μm. Quantifications (right panel; n=3 independent experiments) are presented as mean ± s.d.; *P* values are derived from one-way ANOVA with Dunnett's multiple comparison test.

c, Nuclear morphology in WI-38 cells expressing dominant-negative KASH1 domain (KASH1^{DN}) or depleted of Nesprin1/2 (siNespr1/2), as assessed by Lamin A/C immunostaining. Bar=10 μm.

d, Quantification (related to **c** and Fig. 5d) of nuclear dysmorphia and EGFP-cGAS (perinuclear or nuclear accrual) upon disruption of the LINC complex. Data (n=3 independent experiments) are presented as mean ± s.d.; *P* values are derived from one-way ANOVA with Dunnett's multiple comparison test.

e, Heatmap displaying SASP induction in WI-38 cells expressing dominant negative KASH1 domain (KASH1^{DN}), with or without concomitant STING inhibition (STINGi, 1 μM H-151), as assessed by RT-qPCR.

f, Heatmap displaying SASP induction in LINC-disrupted (siNespr1/2, siSUN1/2) WI-38 cells, as assessed by RT-qPCR.

g, Actin cap disruption (quantification in right panel) coinciding with NE dysmorphia in Nesprin1/2-depleted cells, as visualized by F-Actin and Lamin A/C staining. Bar=10 μm. Data (n=3 independent experiments) are presented as mean ± s.d.; *P* values are derived from two-sided, unpaired *t*-test.

h, Left: RT-qPCR analysis of *LMNB1* expression levels in control (siCo) and YAP/TAZ-depleted (siY/T #1 and #2) WI-38 cells. Right: Immunoblot analysis of Lamin B1 protein levels in WI-38 cells and primary adult fibroblasts (MAFs) upon YAP/TAZ depletion.

i, Heatmap showing cGAS-dependent SASP induction upon Lamin B1 depletion (siLMNB1) in WI-38 cells, as assessed by RT-qPCR.

j, RT-qPCR analysis of SASP marker genes in WI-38 cells upon Lamin B1 (siLMNB1 #1 and #2) or YAP/TAZ (siY/T) depletion.

k, RT-qPCR analysis of *ACTR2* expression levels in control (siCo) and YAP/TAZ-depleted (siY/T #1 and #2) WI-38 cells.

In **h, j, k** data (n=3 independent experiments) are presented as mean ± s.d. *P* values are derived from one-way ANOVA with Dunnett's multiple comparison test.

l, Quantification of actin cap integrity, nuclear dysmorphia and perinuclear EGFP-cGAS accrual upon ACTR2 depletion (siACTR2) in WI-38 cells, 48 hours after transfection. Related to Fig. 5e. Data (n=3 independent experiments) are presented as mean ± s.d.; *P* values are derived from two-sided, unpaired *t*-test.

m, Quantification (left) of mean focal adhesion (FA) length (n=3 independent experiments) and abundance (n=25 cells per condition) upon ACTR2 knockdown in WI-38 cells, 48 hours after siRNA transfection. Data are shown as mean ± s.d.; *P* values are derived from two-sided, unpaired *t*-test. On the right, F-Actin and Vinculin staining (bar=10 μm) in control and ACTR2 -depleted WI-38 cells. Apical and basal sections are shown. IF were taken at 32 hours after siRNA transfection.

n, cGAMP levels in control (siCo) and ACTR2-depleted (siACTR2) WI-38 cells, as assessed by ELISA. Concomitant cGAS depletion served as specificity control. Data (n=3 independent experiments) are shown as mean ± s.d.; *P* values are derived from one-way ANOVA with Dunnett's multiple comparison test.

o, Heatmap showing cGAS-dependent SASP induction upon ACTR2 depletion (siACTR2) in WI-38 cells, as assessed by RT-qPCR.

p, EGFP-cGAS reporter signal (left panel) and quantification (right panel, n=3 independent experiments) in WI-38 cells either control or treated with ARP2/3 inhibitor (ARP2/3i, 50 μM CK-869 for 12 hours). Bar=10 μm. Data are presented as mean ± s.d.; *P* values are derived from two-sided, unpaired *t*-test.

q, RT-qPCR analysis of SASP marker genes in WI-38 cells either control or treated with the ARP2/3 inhibitor (ARP2/3i) CK-869 at the indicated doses. Data (n=3 independent experiments) are presented as mean ± s.d.

r, Quantification of WI-38 cells displaying intact actin cap, nuclear dysmorphia and perinuclear EGFP-cGAS accrual upon YAP/TAZ depletion, with or without concomitant ARPIN depletion. Data (n=3 independent experiments) are shown as mean ± s.d.; *P* values are derived from one-way ANOVA with Dunnett's multiple comparison test. Related to Fig. 5e.

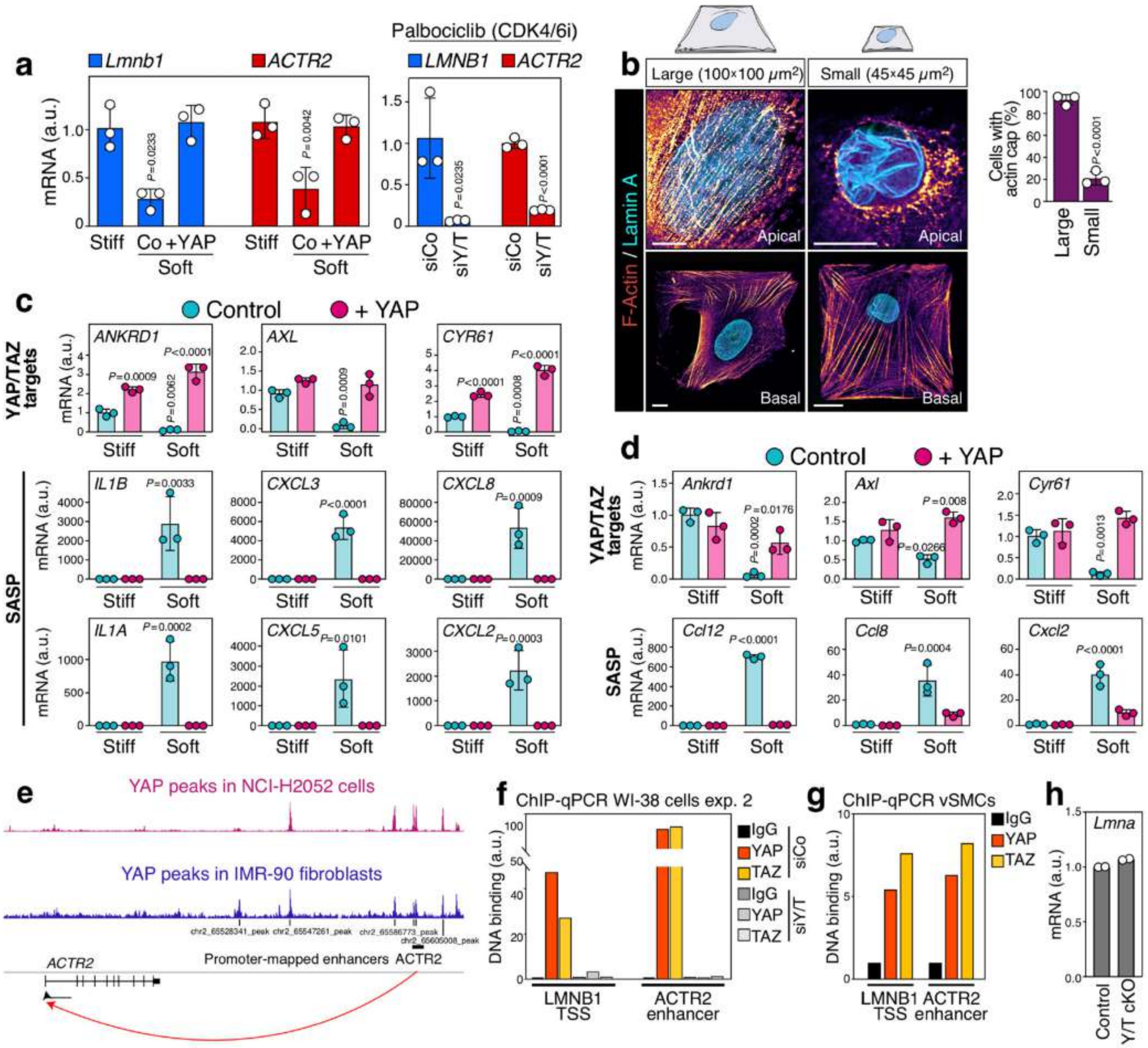

Extended Data Fig. 11. Low mechanics disrupt the nuclear envelope and activate cGAS/STING by inhibiting YAP/TAZ.

a, RT-qPCR analysis (left panel) of *Lmnb1* and *ACTR2* in MAFs and WI-38 cells, respectively, plated on stiff (40 kPa) or soft (0.5 kPa) hydrogels. *Lmnb1* and *ACTR2* expression on soft substrate is rescued by add-back of constitutively active YAP. Of note, cell cycle inhibition (CDK4/6i treatment, 4 μM Palbociclib for 48 hours) in WI-38 cells plated on stiff substrates is inconsequential for *LMNB1* and *ACTR2* expression levels (right panel). Data (n=3 independent experiments) are shown as mean ± s.d.; *P* values are derived from one-way ANOVA with Dunnett's multiple comparison test (left panel) and from two-sided, unpaired *t*-test (right panel).

b, Superresolution microscopy analysis (left panel) of actin cap integrity, as visualized by F-Actin and Lamin A/C staining, and quantification (right panel) in WI-38 cells plated on adhesive microislands of the indicated sizes. Bar=10 μm. Data (n=3 independent experiments) are presented as mean ± s.d.; *P* values are derived from two-sided, unpaired *t*-test.

c, RT-qPCR analysis of YAP/TAZ target genes and SASP marker genes in WI-38 cells plated on stiff (40 kPa) or soft (0.5 kPa) hydrogels in the presence (+YAP) or absence (Control) of constitutively active YAP5SA. Control cells were transduced with empty vector. Data (n=3 independent experiments) are shown as mean ± s.d.; *P* values are derived from one-way ANOVA with Dunnett's multiple comparison test.

d, RT-qPCR analysis of YAP/TAZ target genes and SASP marker genes in primary MAFs plated on stiff (40 kPa) or soft (0.5 kPa) hydrogels. MAFs were isolated from *R26-rtTAM2; Col-tetO-YAPS127A* mice and either left untreated (Control) or treated with doxycycline (+ YAP) ex vivo to sustain YAP activity. Data (n=3 independent experiments) are shown as mean ± s.d.; *P* values are derived from one-way ANOVA with Dunnett's multiple comparison test.

e, ChIP-Seq profiles for YAP in human NCI-H2052 cells and human IMR90 fibroblasts showing YAP binding at enhancer elements mapped (red arrow) to the *ACTR2* promoter, according to published Hi-C interactome maps.

f, Independent repeat experiment of ChIP-qPCR shown in Fig. 5i. Enrichment relative to siY/T: 25.4-fold for TAZ-IP on LMNB1 promoter, 13.8-fold for IP-YAP on LMNB1 promoter; 62.7-fold for IP-TAZ on ACTR2 enhancer, and 99-fold for IP-YAP on ACTR2 enhancer. The panel shows the result of one experiment.

g, ChIP-qPCR analysis in human vascular smooth muscle cells (vSMCs) showing that the regulatory elements for *LMNB1* and *ACTR2* are enriched in YAP- and TAZ-immunoprecipitated chromatin, but not in negative control IP (IgG). Relative DNA binding was calculated as fraction of input and normalized to IgG. The panel shows the result of one experiment, independent repeats for a different cell line (human WI-38) are shown in Fig. 5i and Extended Data Fig. 11f.

h, YAP/TAZ-depletion in primary MAFs is inconsequential for *Lmna* expression levels, as assessed by RNA-Seq. Results of two independent experiments are shown.

Supplementary Material

Refer to Web version on PubMed Central for supplementary material.

Acknowledgments

We thank colleagues sharing their plasmids on Addgene, the IFOM imaging facility team (Dario Parazzoli, Massimiliano Garre', Amanda Oldani, Galina Beznusenko, Alexander Mironov) for advice on image processing; Sandra Soligo, Irene D'Arsiè and Benedetta Marchesan for managing the mouse colony, and all members of our group for reading the MS. We are thankful to Valeria Cancila for support on PLA; Marco Sandri and Libero Vitiello for providing C57BL/6N wild-type mice older than 18 months. H.L.S.-M. was first supported by EMBO ALTF 987-2016 and then by Marie Skłodowska-Curie Individual Fellowship (IF) 798570 - YAP MECHANO; G. Brumana was supported by a Fondazione Cariparo PhD fellowship. The research leading to these results has received funding from the following agencies/charities: Fondazione AIRC under 5 per mille 2019 - ID. 22759 program - P.I. Piccolo Stefano; Fondazione AIRC, IG 2019 - ID. 23307 project – P.I. Piccolo Stefano; the European Research Council (ERC) under the European Union's Horizon 2020 research and innovation program DENOVOSTEM grant agreement No 670126 to S.P.; PRIN-MIUR to S.P., T.P and F.Z (2017HWTP2K, 2017L8FWY8 and 2017JWZKP2, respectively) and Bando Ricerca Scientifica di Eccellenza 2018 Fondazione Cariparo nr. 52008 to G. Brusatin and S.P.

Data availability

All RNA-seq and sc-RNA-seq data generated for the present study are available as GSE165668 at the Gene Expression Omnibus (GEO; https://www.ncbi.nlm.nih.gov/geo/). scRNA-seq data from the *Tabula Muris Senis* atlas were obtained from Gene Expression Omnibus GSE149590. Raw single cell RNA-seq data of mouse skeletal stem cells have been downloaded from Gene Expression Omnibus GSE161946.

Code availability

All code was performed using R 3.5.0 and publicly available packages explicitly cited in the manuscript. No custom functions were written for the analysis. STAR is available in GitHub (https://github.com/alexdobin/STAR).

References

1. Childs BG, et al. Senescent cells: an emerging target for diseases of ageing. Nat Rev Drug Discov. 2017; 16: 718–735. DOI: 10.1038/nrd.2017.116 [PubMed: 28729727]
2. Xu M, et al. Senolytics improve physical function and increase lifespan in old age. Nat Med. 2018; 24: 1246–1256. DOI: 10.1038/s41591-018-0092-9 [PubMed: 29988130]
3. Lopez-Otin C, Blasco MA, Partridge L, Serrano M, Kroemer G. The hallmarks of aging. Cell. 2013; 153: 1194–1217. DOI: 10.1016/j.cell.2013.05.039 [PubMed: 23746838]
4. Ewald CY. The Matrisome during Aging and Longevity: A Systems-Level Approach toward Defining Matreotypes Promoting Healthy Aging. Gerontology. 2020; 66: 266–274. DOI: 10.1159/000504295 [PubMed: 31838471]
5. Ge Y, et al. The aging skin microenvironment dictates stem cell behavior. Proc Natl Acad Sci U S A. 2020; 117: 5339–5350. DOI: 10.1073/pnas.1901720117 [PubMed: 32094197]
6. Panciera T, Azzolin L, Cordenonsi M, Piccolo S. Mechanobiology of YAP and TAZ in physiology and disease. Nat Rev Mol Cell Biol. 2017; 18: 758–770. DOI: 10.1038/nrm.2017.87 [PubMed: 28951564]
7. Kechagia JZ, Ivaska J, Roca-Cusachs P. Integrins as biomechanical sensors of the microenvironment. Nat Rev Mol Cell Bio. 2019; 20: 457–473. DOI: 10.1038/s41580-019-0134-2 [PubMed: 31182865]
8. Meng Z, et al. RAP2 mediates mechanoresponses of the Hippo pathway. Nature. 2018; 560: 655–660. DOI: 10.1038/s41586-018-0444-0 [PubMed: 30135582]
9. Cordenonsi M, et al. The Hippo transducer TAZ confers cancer stem cell-related traits on breast cancer cells. Cell. 2011; 147: 759–772. DOI: 10.1016/j.cell.2011.09.048 [PubMed: 22078877]
10. Tabula Muris C. A single-cell transcriptomic atlas characterizes ageing tissues in the mouse. Nature. 2020; 583: 590–595. DOI: 10.1038/s41586-020-2496-1 [PubMed: 32669714]
11. Tigges J, et al. The hallmarks of fibroblast ageing. Mech Ageing Dev. 2014; 138: 26–44. DOI: 10.1016/j.mad.2014.03.004 [PubMed: 24686308]
12. Humphrey JD, Milewicz DM, Tellides G, Schwartz MA. Cell biology. Dysfunctional mechanosensing in aneurysms. Science. 2014; 344: 477–479. DOI: 10.1126/science.1253026 [PubMed: 24786066]
13. Zheng B, Zhang Z, Black CM, de Crombrugghe B, Denton CP. Ligand-dependent genetic recombination in fibroblasts : a potentially powerful technique for investigating gene function in fibrosis. Am J Pathol. 2002; 160: 1609–1617. DOI: 10.1016/S0002-9440(10)61108-X [PubMed: 12000713]
14. Fisher GJ, Varani J, Voorhees JJ. Looking older: fibroblast collapse and therapeutic implications. Arch Dermatol. 2008; 144: 666–672. DOI: 10.1001/archderm.144.5.666 [PubMed: 18490597]
15. Tchkonia T, et al. Fat tissue, aging, and cellular senescence. Aging Cell. 2010; 9: 667–684. DOI: 10.1111/j.1474-9726.2010.00608.x [PubMed: 20701600]

16. Camargo FD, et al. YAP1 increases organ size and expands undifferentiated progenitor cells. Curr Biol. 2007; 17: 2054–2060. DOI: 10.1016/j.cub.2007.10.039 [PubMed: 17980593]
17. Wirth A, et al. G12-G13-LARG-mediated signaling in vascular smooth muscle is required for salt-induced hypertension. Nat Med. 2008; 14: 64–68. DOI: 10.1038/nm1666 [PubMed: 18084302]
18. Sengle G, Sakai LY. The fibrillin microfibril scaffold: A niche for growth factors and mechanosensation? Matrix Biol. 2015; 47: 3–12. DOI: 10.1016/j.matbio.2015.05.002 [PubMed: 25957947]
19. Salvi P, et al. Aortic dilatation in Marfan syndrome: role of arterial stiffness and fibrillin-1 variants. J Hypertens. 2018; 36: 77–84. DOI: 10.1097/HJH.0000000000001512 [PubMed: 29210860]
20. Bunton TE, et al. Phenotypic alteration of vascular smooth muscle cells precedes elastolysis in a mouse model of Marfan syndrome. Circ Res. 2001; 88: 37–43. DOI: 10.1161/01.res.88.1.37 [PubMed: 11139471]
21. Santinon G, et al. dNTP metabolism links mechanical cues and YAP/TAZ to cell growth and oncogene-induced senescence. EMBO J. 2018; 37 doi: 10.15252/embj.201797780
22. Xu Y, et al. Revealing a core signaling regulatory mechanism for pluripotent stem cell survival and self-renewal by small molecules. Proc Natl Acad Sci U S A. 2010; 107: 8129–8134. DOI: 10.1073/pnas.1002024107 [PubMed: 20406903]
23. Dou Z, et al. Cytoplasmic chromatin triggers inflammation in senescence and cancer. Nature. 2017; 550: 402–406. DOI: 10.1038/nature24050 [PubMed: 28976970]
24. Gluck S, et al. Innate immune sensing of cytosolic chromatin fragments through cGAS promotes senescence. Nat Cell Biol. 2017; 19: 1061–1070. DOI: 10.1038/ncb3586 [PubMed: 28759028]
25. Ablasser A, Chen ZJ. cGAS in action: Expanding roles in immunity and inflammation. Science. 2019; 363 doi: 10.1126/science.aat8657
26. Decout A, Katz JD, Venkatraman S, Ablasser A. The cGAS-STING pathway as a therapeutic target in inflammatory diseases. Nat Rev Immunol. 2021; 21: 548–569. DOI: 10.1038/s41577-021-00524-z [PubMed: 33833439]
27. Zanconato F, et al. Genome-wide association between YAP/TAZ/TEAD and AP-1 at enhancers drives oncogenic growth. Nat Cell Biol. 2015; 17: 1218–1227. DOI: 10.1038/ncb3216 [PubMed: 26258633]
28. Sauer JD, et al. The N-ethyl-N-nitrosourea-induced Goldenticket mouse mutant reveals an essential function of Sting in the in vivo interferon response to Listeria monocytogenes and cyclic dinucleotides. Infect Immun. 2011; 79: 688–694. DOI: 10.1128/IAI.00999-10 [PubMed: 21098106]
29. Haag SM, et al. Targeting STING with covalent small-molecule inhibitors. Nature. 2018; 559: 269–273. DOI: 10.1038/s41586-018-0287-8 [PubMed: 29973723]
30. Larrieu D, Britton S, Demir M, Rodriguez R, Jackson SP. Chemical inhibition of NAT10 corrects defects of laminopathic cells. Science. 2014; 344: 527–532. DOI: 10.1126/science.1252651 [PubMed: 24786082]
31. Khatau SB, et al. A perinuclear actin cap regulates nuclear shape. Proc Natl Acad Sci U S A. 2009; 106: 19017–19022. DOI: 10.1073/pnas.0908686106 [PubMed: 19850871]
32. Kim JK, et al. Nuclear lamin A/C harnesses the perinuclear apical actin cables to protect nuclear morphology. Nat Commun. 2017; 8: 2123. doi: 10.1038/s41467-017-02217-5 [PubMed: 29242553]
33. Maurer M, Lammerding J. The Driving Force: Nuclear Mechanotransduction in Cellular Function, Fate, and Disease. Annu Rev Biomed Eng. 2019; 21: 443–468. DOI: 10.1146/annurev-bioeng-060418-052139 [PubMed: 30916994]
34. Elosegui-Artola A, et al. Force Triggers YAP Nuclear Entry by Regulating Transport across Nuclear Pores. Cell. 2017; 171: 1397–1410. e1314 doi: 10.1016/j.cell.2017.10.008 [PubMed: 29107331]
35. Vergnes L, Peterfy M, Bergo MO, Young SG, Reue K. Lamin B1 is required for mouse development and nuclear integrity. Proc Natl Acad Sci U S A. 2004; 101: 10428–10433. DOI: 10.1073/pnas.0401424101 [PubMed: 15232008]
36. Shimi T, et al. The role of nuclear lamin B1 in cell proliferation and senescence. Genes Dev. 2011; 25: 2579–2593. DOI: 10.1101/gad.179515.111 [PubMed: 22155925]

37. Bedrosian TA, et al. Lamin B1 decline underlies age-related loss of adult hippocampal neurogenesis. EMBO J. 2021; 40 e105819 doi: 10.15252/embj.2020105819 [PubMed: 33300615]

38. Dreesen O, et al. Lamin B1 fluctuations have differential effects on cellular proliferation and senescence. J Cell Biol. 2013; 200: 605–617. DOI: 10.1083/jcb.201206121 [PubMed: 23439683]

39. Shah PP, et al. Lamin B1 depletion in senescent cells triggers large-scale changes in gene expression and the chromatin landscape. Genes Dev. 2013; 27: 1787–1799. DOI: 10.1101/gad.223834.113 [PubMed: 23934658]

40. Goley ED, Welch MD. The ARP2/3 complex: an actin nucleator comes of age. Nat Rev Mol Cell Biol. 2006; 7: 713–726. DOI: 10.1038/nrm2026 [PubMed: 16990851]

41. Dang I, et al. Inhibitory signalling to the Arp2/3 complex steers cell migration. Nature. 2013; 503: 281–284. DOI: 10.1038/nature12611 [PubMed: 24132237]

42. Totaro A, et al. YAP/TAZ link cell mechanics to Notch signalling to control epidermal stem cell fate. Nat Commun. 2017; 8 15206 doi: 10.1038/ncomms15206 [PubMed: 28513598]

43. Nader GPF, et al. Compromised nuclear envelope integrity drives TREX1-dependent DNA damage and tumor cell invasion. Cell. 2021; doi: 10.1016/j.cell.2021.08.035

44. Raab M, et al. ESCRT III repairs nuclear envelope ruptures during cell migration to limit DNA damage and cell death. Science. 2016; 352: 359–362. DOI: 10.1126/science.aad7611 [PubMed: 27013426]

45. Denais CM, et al. Nuclear envelope rupture and repair during cancer cell migration. Science. 2016; 352: 353–358. DOI: 10.1126/science.aad7297 [PubMed: 27013428]

46. Kidiyoor GR, et al. ATR is essential for preservation of cell mechanics and nuclear integrity during interstitial migration. Nat Commun. 2020; 11: 4828. doi: 10.1038/s41467-020-18580-9 [PubMed: 32973141]

47. He C, et al. YAP1-LATS2 feedback loop dictates senescent or malignant cell fate to maintain tissue homeostasis. EMBO Rep. 2019; 20 doi: 10.15252/embr.201744948

48. Fausti F, et al. ATM kinase enables the functional axis of YAP, PML and p53 to ameliorate loss of Werner protein-mediated oncogenic senescence. Cell Death Differ. 2013; 20: 1498–1509. DOI: 10.1038/cdd.2013.101 [PubMed: 23933816]

49. Zanconato F, Cordenonsi M, Piccolo S. YAP/TAZ at the Roots of Cancer. Cancer Cell. 2016; 29: 783–803. DOI: 10.1016/j.ccell.2016.05.005 [PubMed: 27300434]

50. Gurkar AU, Niedernhofer LJ. Comparison of mice with accelerated aging caused by distinct mechanisms. Exp Gerontol. 2015; 68: 43–50. DOI: 10.1016/j.exger.2015.01.045 [PubMed: 25617508]

51. Ambrosi TH, et al. Aged skeletal stem cells generate an inflammatory degenerative niche. Nature. 2021; 597: 256–262. DOI: 10.1038/s41586-021-03795-7 [PubMed: 34381212]

52. Zhang N, et al. The Merlin/NF2 tumor suppressor functions through the YAP oncoprotein to regulate tissue homeostasis in mammals. Dev Cell. 2010; 19: 27–38. DOI: 10.1016/j.devcel.2010.06.015 [PubMed: 20643348]

53. Judge DP, et al. Evidence for a critical contribution of haploinsufficiency in the complex pathogenesis of Marfan syndrome. J Clin Invest. 2004; 114: 172–181. DOI: 10.1172/JCI20641 [PubMed: 15254584]

54. Azzolin L, et al. YAP/TAZ incorporation in the beta-catenin destruction complex orchestrates the Wnt response. Cell. 2014; 158: 157–170. DOI: 10.1016/j.cell.2014.06.013 [PubMed: 24976009]

55. Totaro A, et al. Cell phenotypic plasticity requires autophagic flux driven by YAP/TAZ mechanotransduction. Proc Natl Acad Sci U S A. 2019; 116: 17848–17857. DOI: 10.1073/pnas.1908228116 [PubMed: 31416916]

56. Morsut L, et al. Negative control of Smad activity by ectodermin/Tif1gamma patterns the mammalian embryo. Development. 2010; 137: 2571–2578. DOI: 10.1242/dev.053801 [PubMed: 20573697]

57. Panciera T, et al. Reprogramming normal cells into tumour precursors requires ECM stiffness and oncogene-mediated changes of cell mechanical properties. Nat Mater. 2020; 19: 797–806. DOI: 10.1038/s41563-020-0615-x [PubMed: 32066931]

58. Stuart T, et al. Comprehensive Integration of Single-Cell Data. Cell. 2019; 177: 1888–1902. e1821 doi: 10.1016/j.cell.2019.05.031 [PubMed: 31178118]

59. Wolock SL, Lopez R, Klein AM. Scrublet: Computational Identification of Cell Doublets in Single-Cell Transcriptomic Data. Cell Syst. 2019; 8: 281–291. e289 doi: 10.1016/j.cels.2018.11.005 [PubMed: 30954476]

60. Aran D, et al. Reference-based analysis of lung single-cell sequencing reveals a transitional profibrotic macrophage. Nat Immunol. 2019; 20: 163–172. DOI: 10.1038/s41590-018-0276-y [PubMed: 30643263]

61. Morikawa Y, et al. Actin cytoskeletal remodeling with protrusion formation is essential for heart regeneration in Hippo-deficient mice. Sci Signal. 2015; 8 ra41 doi: 10.1126/scisignal.2005781 [PubMed: 25943351]

62. Hetrick B, Han MS, Helgeson LA, Nolen BJ. Small molecules CK-666 and CK-869 inhibit actin-related protein 2/3 complex by blocking an activating conformational change. Chem Biol. 2013; 20: 701–712. DOI: 10.1016/j.chembiol.2013.03.019 [PubMed: 23623350]

63. Panciera T, et al. Induction of Expandable Tissue-Specific Stem/Progenitor Cells through Transient Expression of YAP/TAZ. Cell Stem Cell. 2016; 19: 725–737. DOI: 10.1016/j.stem.2016.08.009 [PubMed: 27641305]

64. Dobin A, et al. STAR: ultrafast universal RNA-seq aligner. Bioinformatics. 2013; 29: 15–21. DOI: 10.1093/bioinformatics/bts635 [PubMed: 23104886]

65. Liao Y, Smyth GK, Shi W. featureCounts: an efficient general purpose program for assigning sequence reads to genomic features. Bioinformatics. 2014; 30: 923–930. DOI: 10.1093/bioinformatics/btt656 [PubMed: 24227677]

66. Robinson MD, McCarthy DJ, Smyth GK. edgeR: a Bioconductor package for differential expression analysis of digital gene expression data. Bioinformatics. 2010; 26: 139–140. DOI: 10.1093/bioinformatics/btp616 [PubMed: 19910308]

67. Subramanian A, et al. Gene set enrichment analysis: a knowledge-based approach for interpreting genome-wide expression profiles. Proc Natl Acad Sci U S A. 2005; 102: 15545–15550. DOI: 10.1073/pnas.0506580102 [PubMed: 16199517]

68. Yang H, Wang H, Ren J, Chen Q, Chen ZJ. cGAS is essential for cellular senescence. Proc Natl Acad Sci U S A. 2017; 114: E4612–E4620. DOI: 10.1073/pnas.1705499114 [PubMed: 28533362]

69. Coppe JP, Desprez PY, Krtolica A, Campisi J. The senescence-associated secretory phenotype: the dark side of tumor suppression. Annu Rev Pathol. 2010; 5: 99–118. DOI: 10.1146/annurev-pathol-121808-102144 [PubMed: 20078217]

70. Haydont V, Neiveyans V, Zucchi H, Fortunel NO, Asselineau D. Genome-wide profiling of adult human papillary and reticular fibroblasts identifies ACAN, Col XI alpha1, and PSG1 as general biomarkers of dermis ageing, and KANK4 as an exemplary effector of papillary fibroblast ageing, related to contractility. Mech Ageing Dev. 2019; 177: 157–181. DOI: 10.1016/j.mad.2018.06.003 [PubMed: 29913199]

71. Haydont V, Neiveyans V, Fortunel NO, Asselineau D. Transcriptome profiling of human papillary and reticular fibroblasts from adult interfollicular dermis pinpoints the ‘tissue skeleton’ gene network as a component of skin chrono-ageing. Mech Ageing Dev. 2019; 179: 60–77. DOI: 10.1016/j.mad.2019.01.003 [PubMed: 30641112]

72. Kaur A, et al. Remodeling of the Collagen Matrix in Aging Skin Promotes Melanoma Metastasis and Affects Immune Cell Motility. Cancer Discov. 2019; 9: 64–81. DOI: 10.1158/2159-8290.CD-18-0193 [PubMed: 30279173]

73. Mahmoudi S, et al. Heterogeneity in old fibroblasts is linked to variability in reprogramming and wound healing. Nature. 2019; 574: 553–558. DOI: 10.1038/s41586-019-1658-5 [PubMed: 31645721]

74. Salzer MC, et al. Identity Noise and Adipogenic Traits Characterize Dermal Fibroblast Aging. Cell. 2018; 175: 1575–1590. e1522 doi: 10.1016/j.cell.2018.10.012 [PubMed: 30415840]

75. Waldera Lupa DM, et al. Characterization of Skin Aging-Associated Secreted Proteins (SAASP) Produced by Dermal Fibroblasts Isolated from Intrinsically Aged Human Skin. J Invest Dermatol. 2015; 135: 1954–1968. DOI: 10.1038/jid.2015.120 [PubMed: 25815425]

76. Zanconato F, et al. Transcriptional addiction in cancer cells is mediated by YAP/TAZ through BRD4. Nat Med. 2018; 24: 1599–1610. DOI: 10.1038/s41591-018-0158-8 [PubMed: 30224758]

77. Stein C, et al. YAP1 Exerts Its Transcriptional Control via TEAD-Mediated Activation of Enhancers. PLoS Genet. 2015; 11 e1005465 doi: 10.1371/journal.pgen.1005465 [PubMed: 26295846]

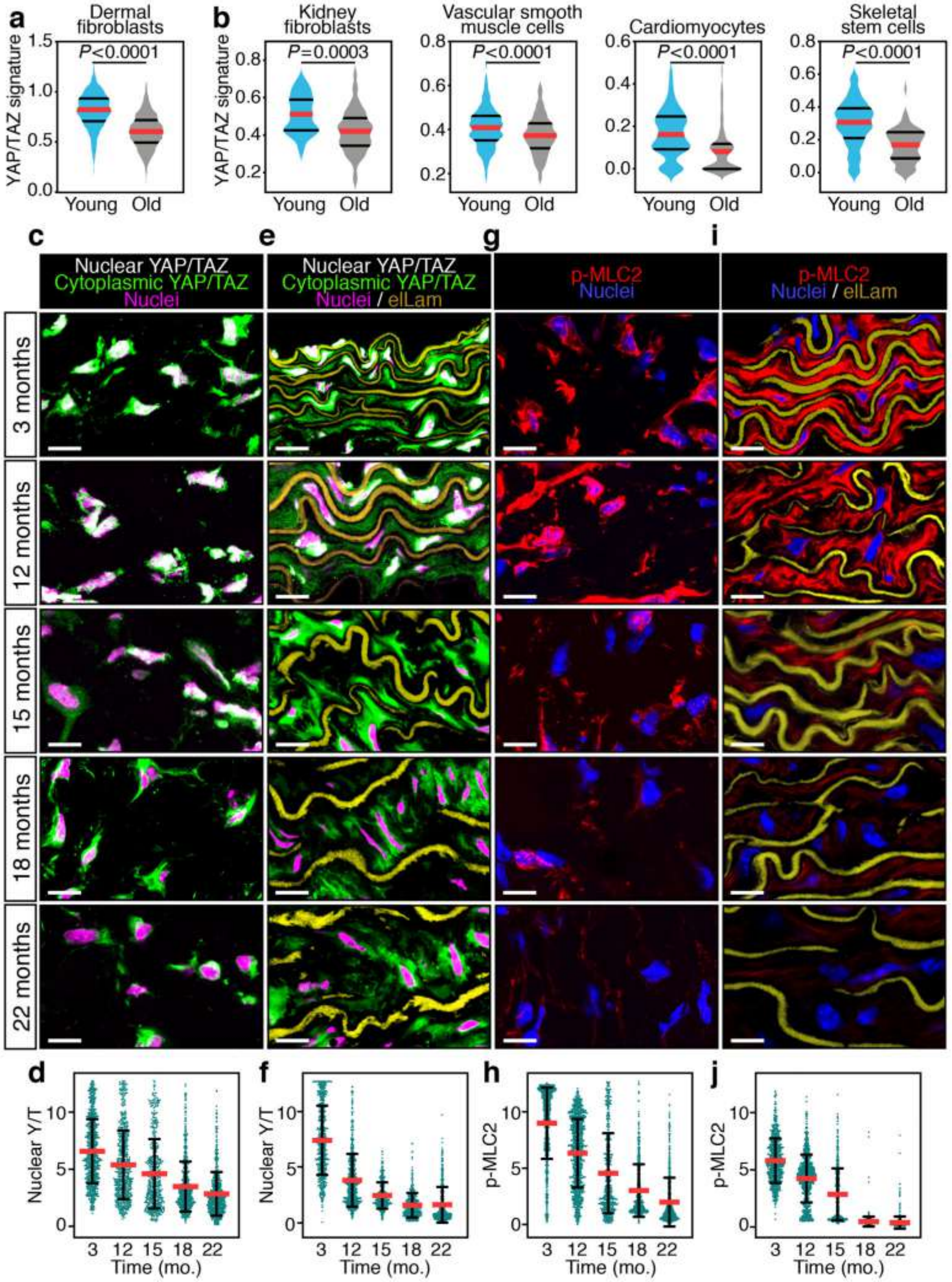

Fig. 1. YAP/TAZ mechanotransduction decreases in connective tissues during natural ageing.

a, Violin plots showing the distribution of YAP/TAZ activity signature expression in freshly dissociated dermal fibroblasts from young (3 months; n=2916 cells) and old (24 months; n=1413 cells) mice, as assessed by scRNA-seq analysis.

b, Violin plots showing the distribution of YAP/TAZ activity signature expression in the indicated cell types from young and old mice. Data were retrieved from *Tabula Muris Senis* for kidney fibroblasts (young n= 28 cells; old n= 84 cells), vascular smooth muscle cells (young n= 472 cells; old n= 362 cells), and cardiomyocytes (young n=100 cells; old n=110 cells) and from Ambrosi et al.[51] for skeletal stem cells (young n= 170 cells; old n= 67 cells). In **a**, and **b**, red lines denote the median, black lines denote quartiles. *P* values are derived from two-sided, unpaired t-test with Welch's correction.

c, e, g, i, Representative immunofluorescence staining for YAP/TAZ and phospho-MLC2 (p-MLC2) in dermal fibroblasts (**c**, **g**) and aortic wall (**e**, **i**) of wild-type mice of the indicated ages. elLam, elastic lamellae. Scale bars, 10 µm. In **c**, and **e**, white signal indicates overlap of YAP/TAZ IF signal (green) with nuclear staining (magenta).

d, f, h, j, Quantification of nuclear YAP/TAZ (Y/T) intensity in dermal fibroblasts (**d**, related to **c**) and aortic smooth muscle cells (**f**, related to **e**) and quantification of the p-MLC2 signal in dermal fibroblasts (**h**, related to **g**) and aortic smooth muscle cells (**j**, related to **i**) of wild-type mice of the indicated ages. Data are shown as mean (red line) ± s.d. At least 400 cells per condition were analyzed from 3 independent mice. *P* values are derived from one-way ANOVA with Dunnett's multiple comparison test. $P<0.0001$ in all conditions compared to 3-month-old mice.

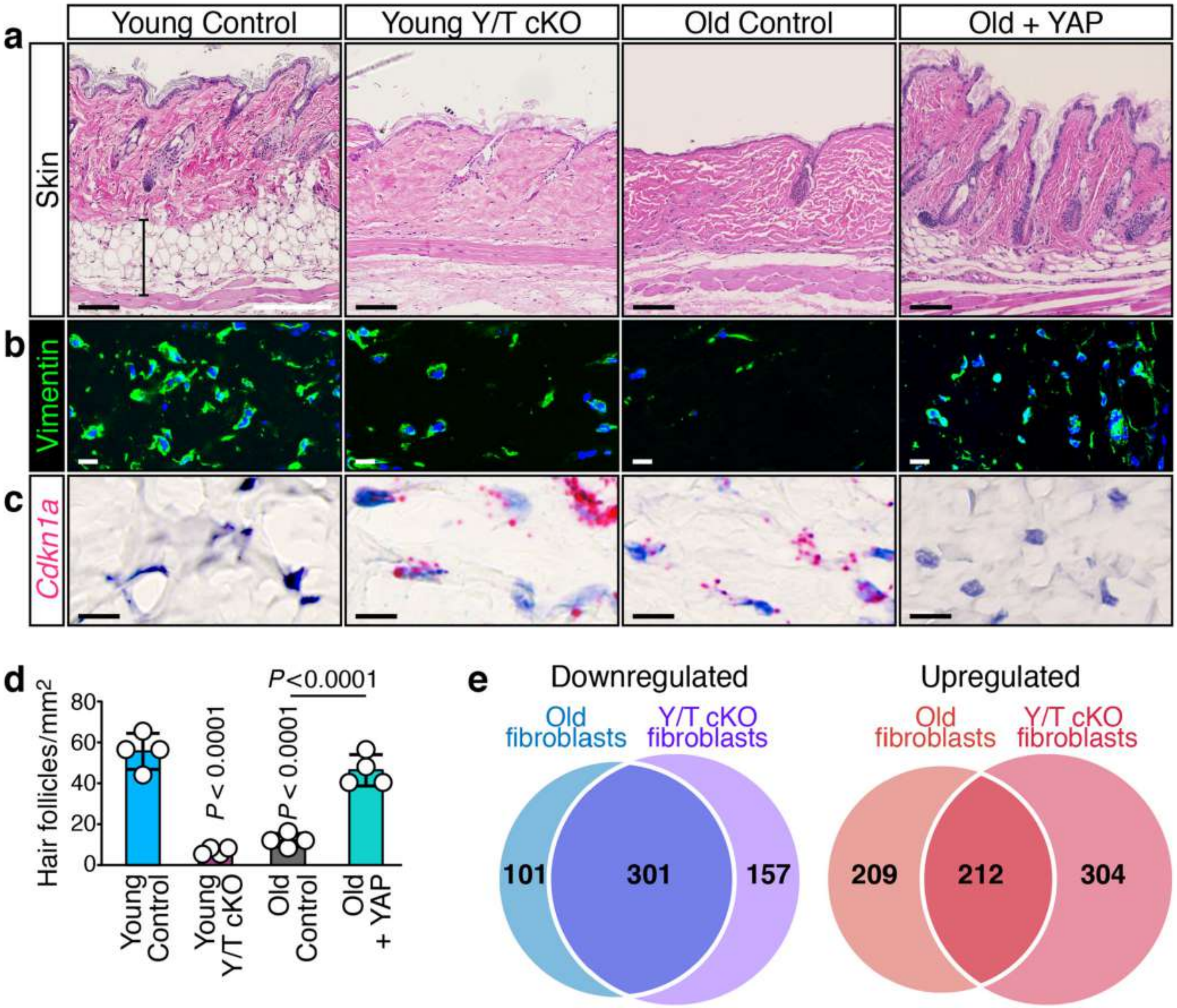

Fig. 2. YAP/TAZ in dermal fibroblasts protect the skin from premature aging.

a-**c**, Left panels are representative images of dorsal skin sections of young (4 months) control and YAP/TAZ knockout mice (Young Y/T cKO); right panels are old (>21 months) control (Old) and age-matched mice where in the latter YAP activity was sustained throughout life (Old + YAP). **a** H&E (bar=100 µm); **b**, IF for Vimentin (scale bar, 10 µm), see Extended Data Fig. 2b for quantification. **c**, *in situ* hybridization for *Cdkn1a* (bar=10 µm), see Extended Data Fig. 2c for quantification. **b** and **c** are enlargements of the dermal layer. Y/T cKO mice were 2.5-month-old *Col1a2-CreER; Yap*$^{fl/fl}$*; Taz*$^{fl/fl}$ treated with Tamoxifen to induce YAP/TAZ deletion in dermal fibroblasts and analyzed 6 weeks later. Old + YAP mice were *R26-rtTAM2; Col-tetO-YAPS127A* mice administered with pulsating doxycycline regime starting at 3 months of age.

d, Quantification of hair follicle density in skin sections from mice of the indicated genotypes. Data (n=4 mice for each column) are presented as mean ± s.d.; *P* values are derived from one-way ANOVA with Dunnett’s multiple comparison test.
e, Venn diagrams depicting genes down- and upregulated in YAP/TAZ cKO (Y/T cKO) and old dermal fibroblasts compared to fibroblasts from young mice, as assessed by scRNA-Seq analyses.

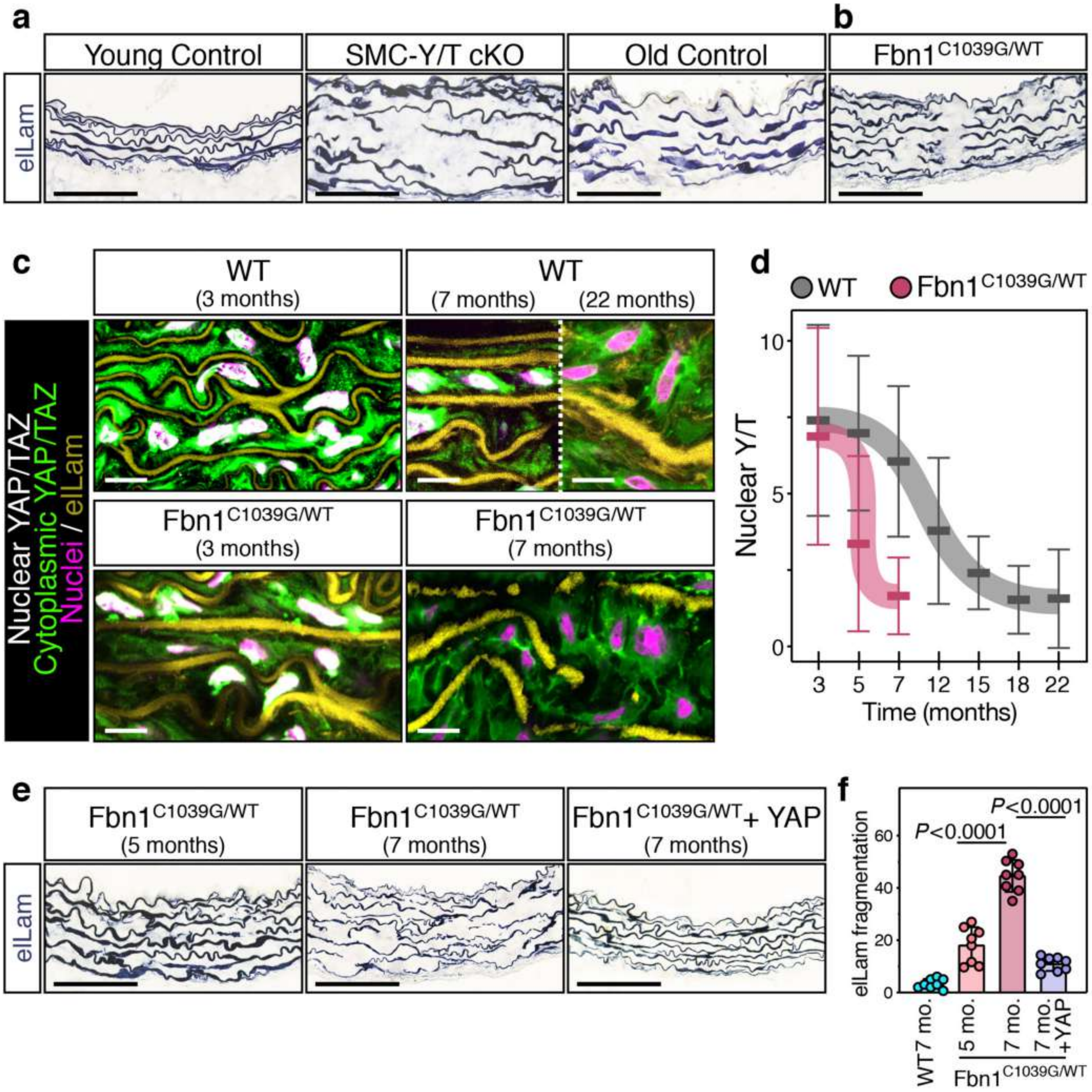

Fig. 3. YAP/TAZ mechanotransduction protects the aortic wall against premature aging.

a, **b**, Representative elastic fiber staining of aortic wall sections of young wild-type (Young Control, 7 months), young SMC-Y/T cKO, old wild-type (Old Control, >21 months) mice (**a**), and young *Fibrillin1* mutant (*Fbn1*$^{C1039G/WT}$, 7 months) mice (**b**). Note comparable degree of elastic lamellae (elLam) fragmentation in young SMC-Y/T cKO, old control and young *Fbn1*$^{C1039G/WT}$ mice. SMC-Y/T cKO were *Smmhc-CreER*^{T2}*; YAP*$^{fl/fl}$*; TAZ*$^{fl/fl}$ mice treated with Tamoxifen to induce YAP/TAZ deletion in vascular smooth muscle cells. Bar=100 μm. See Extended Data Fig. 3c for quantification.

c, **d**, Representative immunofluorescence staining for YAP/TAZ (**c,** bar=10 μm) and quantification (**d**) of nuclear Y/T intensity in the aortic wall of wild-type (WT) and *Fibrillin1* mutant mice of the indicated ages. In **c**, white signal indicates overlap of YAP/TAZ IF signal (green) with nuclear staining (magenta). In **d**, data are displayed as mean ± s.d. *P* values are derived from one-way ANOVA with Dunnett's multiple comparison test. $P<0.0001$ in all conditions compared to 3-month-old wild-type mice, except for 3-month-old *Fibrillin1* mutants ($P=0.0056$). The number of cells analyzed for each mouse strain and age is reported in the corresponding source data file (where n is always >400 cells for each point).

e, **f**, Representative elLam staining (**e**) and quantification (**f**, n=8 mice for each group) of elastic lamellae fragmentation in aortic sections of wild-type (WT 7 months), $Fbn1^{C1039G/WT}$, and $Fbn1^{C1039G/WT}$ mice in which YAP activity was sustained from 5 months of age till sacrifice at 7 months of age ($Fbn1^{C1039G/WT}$ 7 months + YAP). Note worsening of aortic histopathology in $Fbn1^{C1039G/WT}$ mice between 5 and 7 months of age, prevented by YAP add-back over the same time-span. $Fbn1^{C1039G/WT}$ 7 months + YAP were Tamoxifen-treated $Fbn1^{C1039G/WT}$; *Smmhc-CreER*^{T2}; *R26-LSL-rtTA; Col-tetO-YAPS127A* mice also receiving doxycycline 5 days a week. Bar=100 μm. In **f**, data are presented as mean ± s.d.; *P* values are derived from one-way ANOVA with Dunnett's multiple comparison test. See Extended Data Fig. 3g for additional characterization.

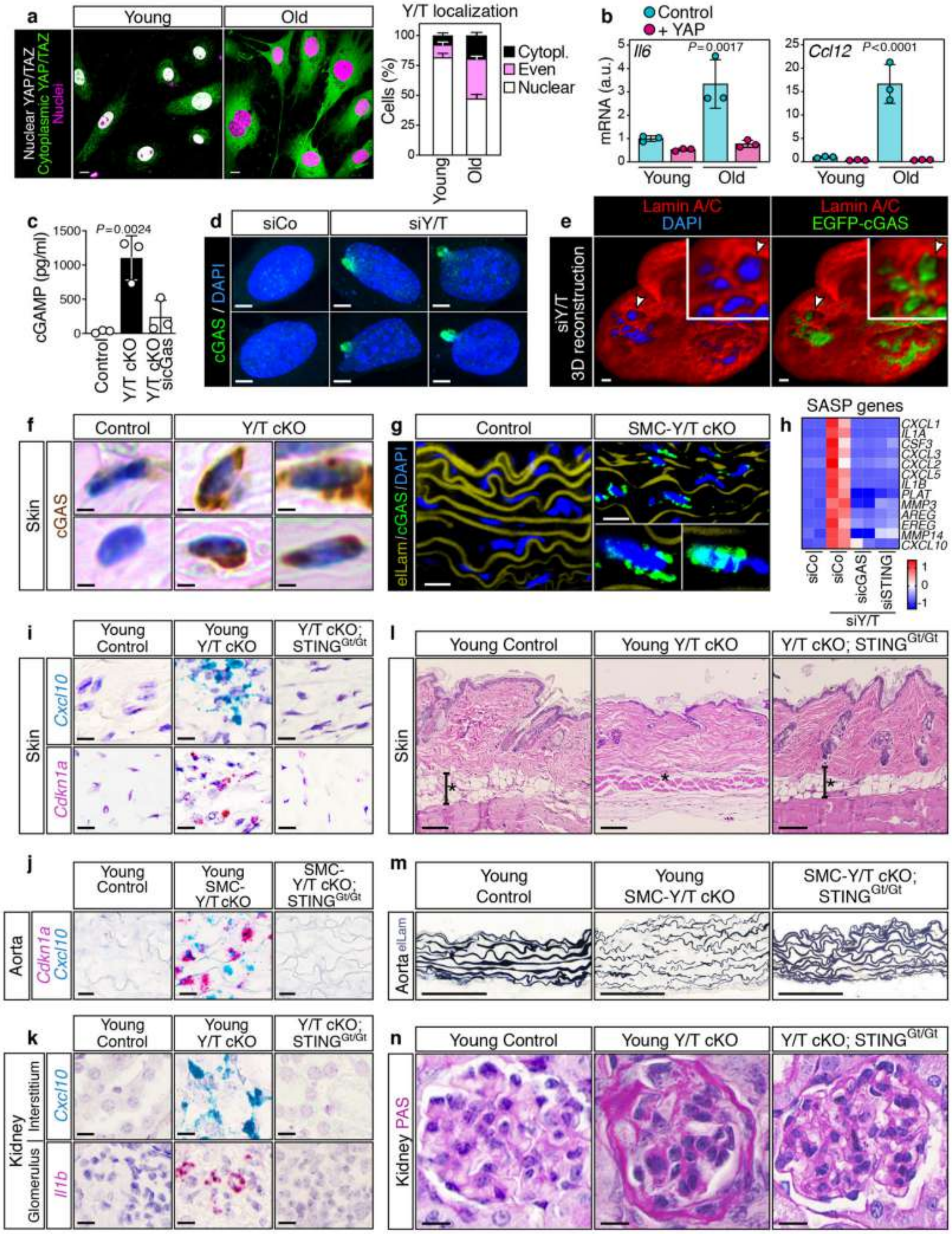

Fig. 4. YAP/TAZ mechanotransduction in stromal cells opposes senescence and aging by inhibiting cGAS-STING signalling.

a, YAP/TAZ immunofluorescence (scale bar, 10 μm) and subcellular quantification (n=3 mice per condition) in freshly isolated young and old (3 versus >21 months) mouse adult fibroblasts (MAFs). Data are mean ± s.d. Cytopl., cytoplasmic.

b, RT-qPCR analysis of SASP markers in young and old MAFs, without and with YAP being added back. Data are mean ± s.d. (n=3 experiments); *P* values are from one-way ANOVA with Dunnett’s multiple comparison test. a.u., arbitrary units.

c, cGAMP quantification in control and YAP/TAZ-depleted MAFs. Data (n=3 experiments) are mean ± s.d.; *P* derived as in **b**.

d, Endogenous cGAS immunofluorescence (scale bar, 1 µm) in control (siCo) and YAP/TAZ-depleted (siY/T) MAFs.

e, 3D reconstruction of a nucleus of YAP/TAZ depleted WI-38 cells expressing EGFP-cGAS and stained with Lamin A/C and DAPI. EGFP-cGAS accrues on exposed genomic DNA (arrowheads). Scale bar, 0.1 µm.

f,**g**, Detection of endogenous cGAS in dermis (f, immunohistochemistry (IHC); scale bar, 1µm) and aortic wall (**g**, immunofluorescence; scale bar, 10µm) of control and YAP/TAZ cKO mice. elLam is elastic lamellae.

h, cGAS- or STING-dependent upregulation of SASP marker genes upon YAP/TAZ depletion in WI-38 cells (RNA-seq heatmap).

i-k, STING is epistatic to YAP/TAZ for the regulation of senescent traits in vivo. Representative ISH for *Cxcl10* and *Cdkn1a* in skin (**i**) and aorta (**j**) sections and *Cxcl10* and *Il1b* in kidney (**k**) interstitial cells and glomerular cells, induced before the onset of tissue degeneration in YAP/TAZ cKO mice. Panels are from age-matched mice of the indicated genotypes. Scale bar, 10 µm. No changes in γH2AX was noted at these time points (Extended Data Fig. 8m).

l-n, Histopathological analysis of skin (**l**, H&E staining; asterisk: subcutaneous fat layer; scale bar, 100 µm), aorta (**m**, elastic fibre staining; scale bar, 100 µm) and kidney (**n**, periodic acid-Schiff staining; scale bar, 10 µm) sections from age-matched young control, YAP/TAZ cKO and compound YAP/TAZ cKO; STING$^{Gt/Gt}$ mice.

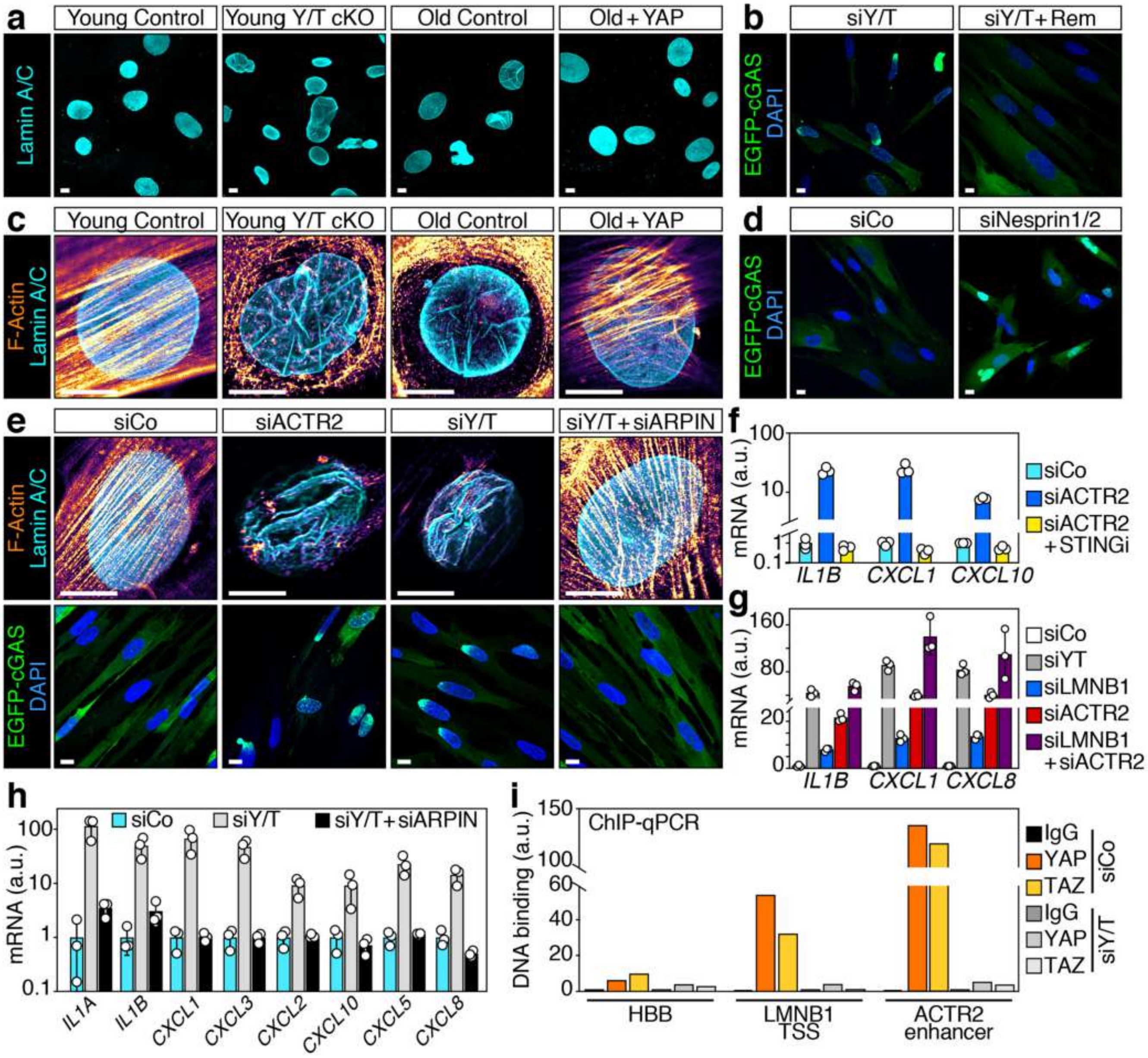

Fig. 5. YAP/TAZ protect the NE through lamin B1 and the actin cap.

a, Nuclear morphology in primary MAFs, as visualized by LaminA/C immunostaining (bar=10 µm). Young MAFs were isolated from *R26-CreER; YAP*$^{fl/fl}$*; Taz*$^{fl/fl}$ mice, left untreated (Young Control) or treated with 4OH-tamoxifen (Y/T cKO) to deplete YAP/TAZ. Old MAFs were isolated from wild-type mice (>21 months) and transduced with either empty vector (Old Control) or doxycycline inducible constitutively active YAP5SA (Old + YAP). See Extended Data Fig. 9a for quantification.

b, EGFP-cGAS reporter signal in YAP/TAZ-depleted (siY/T) WI-38 cells with or without Remodelin treatment (Rem). Bar=10 µm. See Extended Data Fig. 9h for quantification.

c, Superresolution microscopy analysis of actin cap integrity, as visualized by F-Actin and LaminA/C staining, in young (3 months) control and young YAP/TAZ cKO MAFs, or in old

(>21 months) MAFs in presence or absence of constitutively active YAP. Apical sections are shown. Scale bar, 10 µm. See Extended Data Fig. 10a for quantification.

d, EGFP-cGAS reporter signal in control (siCo) and Nesprin1/2-depleted (siNesprin1/2) WI-38 cells. Bar=10 µm. See Extended Data Fig. 10d for quantification.

e, Superresolution microscopy analysis of actin cap integrity (upper row, apical sections are shown), as visualized by F-Actin and LaminA/C staining, and confocal images of EGFP-cGAS reporter signal (lower row) in control (siCo), ACTR2-depleted (siACTR2), YAP/TAZ-depleted (siY/T) or YAP/TAZ/ARPIN-depleted (siY/T+siARPIN) WI-38 cells. Bar=10 µm. See Extended Data Fig. 10l, r for quantification.

f, SASP marker gene expression is induced by ACTR2 depletion (siACTR2) in a STING-dependent manner in WI-38 fibroblasts, as assessed by RT-qPCR. Data (n=3 independent experiments) are shown as mean ± s.d. See Extended Data Fig. 10 p, q for additional data using a small molecule ARP2/3 inhibitor.

g, RT-qPCR for SASP marker genes showing synergistic effects of combined ACTR2 and LaminB1 (siACTR2+siLMNB1) depletion, resembling Y/T depletion (siY/T) in WI-38 fibroblasts. Data (n=3 independent experiments) are presented as mean ± s.d.

h, Expression of SASP markers in YAP/TAZ-depleted WI-38 cells is prevented by concomitant depletion of the endogenous ARP2/3 inhibitor ARPIN. Data (n=3 independent experiments) are shown as mean ± s.d.

i, Representative ChIP-qPCR experiment in WI-38 cells showing that the regulatory promoter/enhancer elements of *LMNB1* and *ACTR2* are enriched in YAP- and TAZ-immunoprecipitated chromatin, but not in negative control IP (IgG) or in chromatin obtained from YAP/TAZ-depleted cells. Relative DNA binding was calculated as fraction of input and normalized to IgG. Enrichment relative to siY/T: 30-fold for TAZ-IP on *LMNB1* promoter, 13.7-fold for IP-YAP on *LMNB1* promoter; 32.7-fold for IP-TAZ on *ACTR2* enhancer, and 26.6-fold for IP-YAP on *ACTR2* enhancer. The panel shows the result of one representative experiment, see Extended Data Fig. 11f-g for an independent repeat and consistent results in vSMCs. In Extended Data Fig. 11h, we show that YAP/TAZ do not regulate the expression of LaminA. TSS, transcription start site.